# Finding Periodic Orbits in Projected Quantum Many-Body Dynamics

Elena Petrova, 1,\* Marko Ljubotina, 1,2,3 Gökhan Yalnız, 1 and Maksym Serbyn, 1

<sup>&</sup>lt;sup>3</sup> Munich Center for Quantum Science and Technology (MCQST), Schellingstr. 4, 80799 München, Germany



(Received 23 April 2025; revised 31 August 2025; accepted 25 September 2025; published 12 November 2025)

Describing general quantum many-body dynamics is a challenging task due to the exponential growth of the Hilbert space with system size. The time-dependent variational principle (TDVP) provides a powerful tool to tackle this task by projecting quantum evolution onto a classical dynamical system within a variational manifold. In classical systems, periodic orbits play a crucial role in understanding the structure of the phase space and the long-term behavior of the system. However, finding periodic orbits is generally difficult, and their existence and properties in generic TDVP dynamics over matrix product states have remained largely unexplored. In this work, we develop an algorithm to systematically identify and characterize periodic orbits in TDVP dynamics. Applying our method to the periodically kicked Ising model, we uncover both stable and unstable periodic orbits. We characterize the Kolmogorov-Arnold-Moser tori in the vicinity of stable periodic orbits and track the change of the periodic orbits as we modify the Hamiltonian parameters. We observe that periodic orbits exist at any value of the coupling constant of the kicked Ising model between prethermal and fully thermalizing regimes, but their relevance to quantum dynamics and imprint on quantum eigenstates diminishes as the system leaves the prethermal regime. Our results demonstrate that periodic orbits provide valuable insights into the TDVP approximation of quantum many-body evolution and establish a closer connection between quantum and classical chaos.

### DOI: 10.1103/tldp-kvkd

## I. INTRODUCTION

The study of quantum chaos has traditionally focused on few-body quantum systems with well-defined semiclassical limits, drawing parallels between classical and quantum dynamics [1]. A central diagnostic of chaos is provided by level statistics [2,3] and out-of-time-ordered correlators [4-7], which do not require an underlying semiclassical description. Early works have explored these criteria in systems with classical counterparts, but recent advances in quantum simulation have shifted attention toward discrete quantum many-body systems, such as spin-1/2 chains, which, at first glance, are far from any semiclassical description.

Although far from the usual semiclassical limit, generic quantum models with small local Hilbert spaces are still expected to be chaotic, as is often probed by their level

Published by the American Physical Society under the terms of the Creative Commons Attribution 4.0 International license. Further distribution of this work must maintain attribution to the author(s) and the published article's title, journal citation, and DOI.

statistics [8–10]. Typical dynamics in such models lead to rapid equilibration, where the system forgets the details of the initial state, relaxing to a state determined only by values of globally conserved quantities, such as energy—a process known as thermalization. Despite recent progress in experiments [11–15] and numerical studies [16–19], understanding chaos and thermalization in discrete interacting quantum systems remains an open and active area of research.

To investigate the dynamics of these many-body quantum systems, matrix product states (MPSs) have emerged as a powerful numerical tool [20,21]. Unlike the manifold of all possible product states, MPSs systematically incorporate short-range entanglement, making them a more expressive variational class. Several methods exist for approximating full unitary quantum dynamics using MPSs [22-24], with the TDVP [25-28] standing out due to its special properties.

It has already been observed by Dirac that the TDVP naturally leads to a symplectic classical dynamical system [25]. When the TDVP is applied to project dynamics onto the manifold of MPSs, it provides a unique perspective: the quantum unitary evolution can be mapped onto an effective classical system that includes additional

<sup>&</sup>lt;sup>1</sup>Institute of Science and Technology Austria (ISTA), Am Campus 1, 3400 Klosterneuburg, Austria <sup>2</sup>Physics Department, Technical University of Munich, TUM School of Natural Sciences, Lichtenbergstr. 4, 85748 Garching, Germany

<sup>\*</sup>Contact author: ptrva1998@gmail.com

entanglement-related degrees of freedom, with the bond dimension (rank) of the MPS,  $\chi$ , controlling the amount of entanglement. This perspective provides a bridge between classical and quantum chaos, where tools from dynamical systems theory can be applied to study quantum thermalization, integrability, and emergent classical-like structures within quantum dynamics.

The emergence of classical dynamical systems from TDVP projections onto the MPS manifold motivates a systematic exploration of their properties [19,29,30]. However, these systems are typically high-dimensional: for a spin-1/2 system, the TDVP, even with the simplest nontrivial bond dimensions  $\chi = 2, 3, ...$ , results in a classical system with  $\chi^2 = 4, 9, \dots$  pairs of canonical coordinates and momenta. Classical chaos theory suggests that periodic orbits serve as fundamental structures that organize the phase space of a system [31–34], providing crucial insights into stability, transport, and ergodicity [35]. For classical systems, periodic orbits are treated as boundaryvalue problems for systems of ordinary differential equations, and well-established numerical algorithms exist for detecting periodic orbits [36–38]. Despite their importance, periodic orbits in generic TDVP-MPS dynamics have remained largely unexplored due to the challenges of identifying them in high-dimensional systems, where symmetries and gauge invariance complicate the navigation of the phase space for the search for periodic orbits [31].

In this work, we formulate and implement a general algorithm to search for periodic orbits within the MPS variational manifold. Using the kicked Ising model [9,18,39–51]—a paradigmatic model for studying quantum thermalization—as an example, we identify periodic orbits and classify them in terms of their stability by computing their Floquet multipliers. For stable orbits, we visualize the surrounding Kolmogorov-Arnold-Moser (KAM) tori [52-55] and show that their dimensionality scales as  $\chi^2$ , in agreement with expectations. Then, we track the change of these periodic orbits as system parameters tune the kicked Ising model from a prethermal regime [56] to a maximally chaotic dual-unitary point [39–43]. In the prethermal regime, we demonstrate that our approach can find variational approximations to eigenstates of the unitary operator generating dynamics over one period in the thermodynamic limit. As the system approaches the chaotic point, periodic orbits do not vanish but become unstable, shifting toward highly entangled regions of the MPS manifold, where entanglement reaches its maximal allowed value given the bond dimension, and leakage is typically higher.

Our findings establish that periodic orbits are present in TDVP-based projections of quantum many-body dynamics onto MPS manifolds. These orbits, both stable and unstable, offer a new perspective on quantum thermalization, providing direct links between quantum and classical chaos. Understanding their structure with increasing bond

dimension offers a promising route to uncovering deeper connections between integrability, chaos, and entanglement in quantum many-body systems.

### II. METHOD FOR PERIODIC ORBITS SEARCH

In this section, we discuss the building blocks of the algorithm used to find periodic orbits. First, we introduce the MPS representation of the wave function and the TDVP that we use to project the dynamics of quantum systems onto the MPS manifold. After this, in Sec. II B we explain the main idea behind the algorithm for periodic orbit search, delegating the detailed description to Appendix A.

# A. iMPS and time-dependent variational principle

The MPS [57] representation of a wave function may be viewed as a systematic improvement of uncorrelated product states that introduces entanglement. In the MPS *Ansatz*, the state is expressed as a contraction of tensors,

$$A_{ij}^s = i - A - j,$$

$$S$$
(1)

with bond indices i and j having bond dimensions  $\chi_1$  and  $\chi_2$ , and the physical index s running over d values corresponding to the local Hilbert-space dimension. We fix d=2, corresponding to spin-1/2, for the rest of this work. For finite systems, each physical degree of freedom is assigned a different tensor within the MPS Ansatz, potentially making translational symmetry difficult to identify. In contrast, the infinite MPS (iMPS) [24,28] explicitly resolves translational invariance by employing a single tensor  $\chi \times d \times \chi$  that repeats infinitely, thus describing translationally invariant states in the thermodynamic limit:

$$|\Phi(A)\rangle = \cdots \qquad A \qquad A \qquad A \qquad A \qquad A \qquad \cdots$$

$$S_{D-1} \qquad S_{D-1} \qquad S_{D-1} \qquad S_{D-1} \qquad S_{D-1}$$

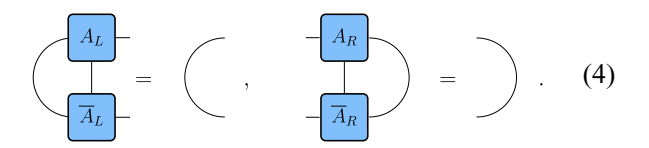
$$(2)$$

The MPS representation of a wave function is not unique, as different choices of tensors  $A_{ij}^s$  can still describe the same state. This nonuniqueness is known as the gauge freedom of MPS. To partially fix the gauge in Eq. (2), we use the mixed-canonical form of the iMPS, which is given by

$$|\Phi(A_L, A_C, A_R)\rangle = \cdots - A_L - A_L - A_C - A_R - A_R - \cdots,$$

$$s_{n-1} \quad s_n \quad s_{n+1}$$
(3)

where tensors  $A_L$  and  $A_R$  obey the orthogonality conditions



Tensors  $A_L$ ,  $A_C$ , and  $A_R$  are obtained from the one tensor A from Eq. (2), and both forms, Eqs. (2) and (3), represent the same physical state. Another tensor that we are going to use in this work is the tensor C, which is defined as  $(A_L)_{ii}^s C_{jk} = (A_C)_{ik}^s$ , where summation over repeated indices is implied. Tensor C allows us to express the MPS state through tensors  $A_L$  and  $A_R$ , and store the information about the bipartite-entanglement entropy of the state. Naively, the number of variables of an iMPS with a given bond dimension  $\chi$  corresponds to the total number of entries in the tensor, i.e.,  $d\chi^2$  complex numbers. However, due to gauge transformations that leave the physical state invariant, not all of these parameters are physically meaningful. After accounting for this redundancy by, e.g., imposing the left- or right-canonical conditions, the number of complex-valued variables describing the iMPS reduces to  $(d-1)\chi^2$ .

Another key concept relevant to our work is the iMPS tangent space. First, the tangent space is used in the TDVP algorithm to perform the time evolution. Second, we are using a tangent-space basis in our gradient-descent algorithm to compute gradients. The tangent space for the iMPS is defined as the set of all possible infinitesimal changes of the iMPS that correspond to physical changes of the quantum state. The most general form of the tangent vector has the following form:

$$|\Phi(V, A_L, A_R)\rangle = \sum_{n} \cdots - A_L - A_L - V - A_R - A_R - \cdots , \quad (5)$$

where tensor V parametrizes directions in the tangent space. We leave the detailed discussion of the construction of the tangent space to Appendix A 2. Here, we only introduce the tangent basis as two sets of tensors  $\{V_{\rm re}^{(\alpha)}\}$  and  $\{V_{\rm im}^{(\alpha)}\}$ , which satisfy the relation

$$iV_{\rm re}^{(\alpha)} = V_{\rm im}^{(\alpha)},\tag{6}$$

where index  $\alpha$  runs over  $\alpha \in [1, (d-1)\chi^2]$ .

To simulate the dynamics of the quantum state, we employ the TDVP algorithm for the iMPS in the mixed gauge. The core idea of this method is to project the action of the Hamiltonian H onto the MPS tangent space, thus ensuring that the state evolution remains within the MPS manifold. Directly applying the Hamiltonian to a state drives it out of the MPS manifold, and the TDVP performs the orthogonal projection back to the MPS tangent space.

By making an orthogonal projection to the MPS tangent space at each step, the TDVP provides an approximation of the full quantum evolution restricted to the variational manifold. The TDVP equation for the quantum system is derived from the projected Schrödinger equation:

$$\partial_t |\psi(A_L, A_C, A_R)\rangle = -i\mathcal{P}H|\psi(A_L, A_C, A_R)\rangle, \tag{7}$$

where  $\mathcal{P}$  here projects the action of the Hamiltonian on the state to the tangent-space manifold, approximating the derivative of the full Schrödinger equation.

The presence of the projector onto the MPS tangent space in Eq. (7) above transforms the otherwise linear Schödinger equation into a highly nonlinear differential equation. In terms of iMPS tensors, these equations of motion can be expressed as follows:

$$\dot{A}_C = -iG_1(A_C),\tag{8a}$$

$$\dot{C} = iG_2(C), \tag{8b}$$

where  $G_1$  and  $G_2$  are linear Hermitian maps that implement the action of the projected Hamiltonian on the state. Although, as written, the equations for  $A_C$  and C look decoupled, in reality, they are interdependent. Indeed, as we discuss in Appendix A 2 (see also reviews [57,58]), the linear Hermitian maps depend on tensors  $A_{L,R}$ , which can be obtained only from knowing both  $A_C$  and C. We note that the TDVP projection of unitary dynamics leads to symplectic classical dynamics, meaning that it preserves the symplectic structure of phase space, ensuring the conservation of fundamental geometric properties [59]. In particular, the TDVP dynamics preserve the phase volume. While the presence of symplectic structure in the equations of motion [Eq. (8)] is not apparent, its consequences will be demonstrated below.

Since the TDVP projects the true quantum dynamics onto the MPS manifold, some information inevitably gets lost over long-time evolution. This is related to the instantaneous leakage [19,30], which is defined as

$$\gamma^{2}(t) = ||\dot{\psi}\rangle + iH|\psi\rangle||^{2} = ||\mathcal{P}H|\psi\rangle - H|\psi\rangle||^{2}, \quad (9)$$

where  $|\psi\rangle$  is a state in the MPS manifold. The leakage is fundamentally linked to entanglement growth as an MPS with a fixed bond dimension  $\chi$  can only accurately represent states with limited entanglement, which is upper bounded by  $S_{\rm ent} \leq \ln \chi$  (here and below, entanglement is defined as the von Neumann entanglement entropy of the reduced density matrix  $\rho_{1/2}$  of half of the system:  $S_{\rm ent} = -\operatorname{tr} \rho_{1/2} \ln \rho_{1/2}$ ). However, during real-time dynamics, the entanglement entropy of a generic interacting quantum system is expected to grow linearly in time [60]. Thus, as exact unitary dynamics would tend to depart from the MPS manifold of a fixed bond dimension—a phenomenon quantified by the leakage—this also leads to

additional entanglement growth compared to that predicted by the TDVP. The leakage computation involves evaluating observables containing products of three operators, such as  $\langle \psi | HPH | \psi \rangle$ , which poses a nontrivial challenge in the iMPS framework due to the infinite nature of the system and the complexity of handling nonlocal operator contractions. Therefore, in this work, we compute the entanglement entropy from numerically exact time evolution and compare it with TDVP predictions to understand how leaky trajectories are.

### B. Gradient-descent method for periodic orbits

To find periodic orbits, we need a reliable way to compare MPSs to determine their similarity. For this purpose, we introduce a measure of distance between two states (fidelity) using the mixed transfer matrix defined for two iMPSs specified by tensors  $A_i$  and  $A_j$  as follows:

$$TM(A_i, A_j) = \begin{pmatrix} -A_i \\ -A_j \\ -\overline{A_j} \end{pmatrix}, \qquad (10)$$

where  $\overline{A}$  denotes complex conjugate tensor. Merging the left and right indices allows us to represent  $TM(A_i, A_j)$  as a  $\chi^2 \times \chi^2$  matrix and study its spectra. In what follows, we focus on injective normalized MPSs [61,62] which have a *unique dominant eigenvalue* of the transfer matrix TM(A, A) with magnitude 1 [63]. Having two such states specified by tensors  $A_i$  and  $A_j$ , we define the fidelity density (fidelity per site, hereafter referred to simply as fidelity) as

$$\mathcal{D}(A_i, A_i) = \rho[\text{TM}(A_i, A_i)], \tag{11}$$

where  $\rho[\cdot]$  denotes the spectral radius, i.e., the largest absolute value among the eigenvalues of the transfer matrix. This function is invariant with respect to MPS gauge transformations. Nevertheless, we will be using a left-canonical form of tensors in what follows. When  $\mathcal{D}(A_i, A_j) = 1$ , the two MPSs  $(A_i \text{ and } A_j)$  represent the same state in the thermodynamic limit. Additional information about the properties of the transfer matrix can be found in Ref. [64].

To find periodic orbits, we want to maximize the fidelity between the initial and time-evolved states. The evolved state is obtained as  $A_L(T) = U_T^{\text{TDVP}}(A_L)$ , where the  $U_T^{\text{TDVP}}(\cdot)$  is the TDVP time propagation to time T according to Eq. (7). Using the fidelity density introduced above, we define the cost function as the fidelity between the initial state and its time-evolved counterpart:

$$F(A_L) = \mathcal{D}(U_T^{\text{TDVP}}(A_L), A_L). \tag{12}$$

In this notation, finding a closed orbit of the Floquet system with fixed period T is equivalent to finding an initial

tensor  $A_L(0)$  such that  $F(A_L(0)) = 1$  (optimization over the period and corresponding results for the Hamiltonian systems we discuss in Appendix D). A naive approach to finding the periodic orbit would be to apply a standard gradient-based optimization algorithm to maximize the cost function in Eq. (12). However, the MPS has redundancies due to the gauge freedom, and such a naive approach will also calculate gradients corresponding to the gauge directions that do not change the quantum state. This results in an additional overhead (e.g., for spin-1/2 systems, the MPS has  $4\chi^2$  real parameters, however, the tangent space has only  $2\chi^2$  independent vectors), and also leads to spurious flat directions in the optimization landscape.

Therefore, in our algorithm, we maximize the cost function in Eq. (12) by restricting the gradients to the MPS tangent-space basis, improving computational efficiency and avoiding the unphysical directions. We use the tangent-space-basis construction discussed in Sec. II A and apply the central-difference method to compute the gradient. We combine the gradient components into an update term  $\delta A_L$ , summing each gradient component with the corresponding basis vector. The overall scheme for calculating an update for the tensor  $A_L$ ,  $\delta A_L$ , is the following:

$$g_{\text{re,im}}^{\alpha} = \frac{F(A_L + \Delta V_{\text{re,im}}^{(\alpha)}) - F(A_L - \Delta V_{\text{re,im}}^{(\alpha)})}{2\Delta},$$

$$\delta A_L = \sum_{\alpha} (g_{\text{re}}^{\alpha} + ig_{\text{im}}^{\alpha}) V_{\text{re}}^{(\alpha)},$$
(13)

where  $V_{\text{re,im}}^{(\alpha)}$  are the tangent space basis vectors from Sec. II A, and we have used Eq. (6) to simplify the second equation. Here we work only with the left-canonical  $(A_L)$  form, as we use the left gauge fixing for the tangent basis, but a similar procedure is also possible for the right-canonical form and corresponding tangent-space basis.

In Eq. (13),  $\delta A_L$  plays the role of the direction along which the tensor  $A_L$  should be updated. To ensure numerical stability, we normalize  $\delta A_L$  by dividing it by the square root of the largest eigenvalue of its transfer matrix  $TM(\delta A_L, \delta A_L)$ . Then, the tensor  $A_L$  is updated by the normalized  $\delta \tilde{A}_L$  times the learning rate c,

$$\tilde{A}_L = A_L + c\delta \tilde{A}_L. \tag{14}$$

The learning rate c is adjusted adaptively during optimization: to mitigate slow convergence in flat regions, whenever the learning rate leads to an improvement in the cost function during the current iteration, we increase it by a factor of  $\xi$ . Conversely, if the current learning rate is too large, causing the update step to fail in improving the objective function, we iteratively reduce it by a factor of  $\tau$  until a valid update step is found. Finally, if the learning

rate shrinks to very small values below a certain threshold, the algorithm is halted. We summarize this procedure as Algorithm 4 in Appendix A 3.

#### III. RESULTS

In this section, we present the results of the periodic orbit search with the tangent-space gradient-descent algorithm. First, in Sec. III A we introduce the kicked Ising model used in our example. Next, in Sec. III B, we present the periodic orbits identified by our algorithm for different values of bond dimension, analyze their stability, and visualize the KAM tori surrounding the stable orbits. After this, in Sec. III C we study the deformation of the periodic orbits as we vary the coupling strengths of the Ising model and discuss the relation between periodic orbits and the eigenstates of the unitary propagator of the quantum model.

### A. Kicked Ising model

To demonstrate the application of our general algorithm for finding periodic orbits, we must choose a specific quantum model. Specifically, we consider a translationally invariant chain of spin-1/2 degrees of freedom, the dynamics of which are described by the kicked Ising model (to avoid confusion, we reserve the use of the term "Floquet" to describe properties of periodic orbits except in Sec. IV). The model can be described by the following translationally invariant Hamiltonian that is periodic in time:

$$H(t) = \begin{cases} H_1 = \sum_i J \sigma_i^z \sigma_{i+1}^z + h \sigma_i^z, & t \bmod T \in [0, T/2), \\ H_2 = \sum_i g \sigma_i^x, & t \bmod T \in [T/2, T), \end{cases}$$

$$(15)$$

where  $\sigma_i^{x,y,z}$  are Pauli matrices. In our work, we fix the z-direction magnetic field h=1, set the period T=1, and choose the two remaining couplings to be equal to each other, g=J, leaving only a single parameter (J). The quantum dynamics of this model over one period is described by the unitary operator

$$U_T = \exp\left(-i\frac{1}{2}H_2\right) \exp\left(-i\frac{1}{2}H_1\right). \tag{16}$$

This will be used below to compare the eigenvalues of  $U_T$  to the periodic orbits identified from the TDVP.

We note that the TDVP algorithm and our orbit-finding method are not sensitive to the time dependence of the Hamiltonian and can be applied in both time-constant and time-dependent settings. However, considering a driven system where the Hamiltonian is time periodic has the advantage of fixing the period of the periodic orbits to be multiples of the driving period. Therefore, the driven setting slightly simplifies the search for periodic orbits, by removing the requirement to optimize for an *a priori* unknown orbit period. An additional advantage of considering the driven system is the absence of any conservation laws, as the time dependence of the Hamiltonian breaks the conservation of energy. As a result, the kicked Ising model in Eq. (15) exhibits translation invariance, which is naturally incorporated through the iMPS *Ansatz*. In addition, it possesses a discrete spatial inversion symmetry and no other conservation laws or symmetries.

The kicked Ising model in Eq. (15) has actively been studied in the literature in the context of quantum thermalization and has several special points in the parameter space. First, when  $J = g = \pi/2$ , the model in Eq. (15) is known to be maximally chaotic. This is the so-called dual-unitary point, where the two-site unitary gates that constitute the building blocks of the unitary propagator  $U_T$  have a special property of maintaining unitarity when one swaps spatial and temporal directions [39–43]. The dual-unitary property allows one to obtain exact results for certain properties of the model, such as the correlation functions [41] and spectral form factor [40]. These exact results suggest that, at this point, parts of the system act as an ideal Markovian bath for the remaining degrees of freedom [44].

Upon reducing the coupling J = g away from the unitary point,  $J = g = \pi/2$ , the model no longer admits treatment with analytical techniques. Nevertheless, numerical studies [44] suggest that the model stays chaotic for coupling J = g not too far away from  $\pi/2$ . This is witnessed by the properties of eigenstates of the unitary operator,  $U_T$ , defined in Eq. (16). The eigenstates, encoding infinite-time properties of the system, feature large volume-law entanglement and small expectation values of all local observables, consistent with the expectations from thermalization to infinite temperature [9,45–48] (see also Appendix C1). Upon decreasing the coupling further, due to the fact that we keep the period and h fixed, the model enters the so-called prethermal regime where the coupling J = g takes the role of an effective small parameter. In this regime, an effective prethermal Hamiltonian can describe the behavior of the system over extended periods before heating effects drive the system toward infinite temperature [49,50]. The prethermal phase depends on system size, and at sufficiently large system sizes, it ceases to exist. The model has also been studied experimentally at the dual-unitary point, repeating analytical calculations, and beyond [65].

Recently, additional insights into the prethermal regime and the existence of an effective prethermal Hamiltonian have been obtained using geometric Floquet theory [18]. In Ref. [18], it is revealed that many of the long-standing features of periodically driven systems, such as quasienergy folding and ambiguities in state ordering, come from a broken gauge symmetry in the adiabatic gauge potential.

Related research shows that the kicked Ising Hamiltonian maintains a low entangled eigenstate—the ground state (GS) of the effective Floquet Hamiltonian—that avoids heating up to some values of J [51]. In the following, we will argue that our method for finding periodic orbits gives complementary insights into the prethermal regime and we discuss our findings in the context of the earlier works.

## B. Periodic orbits, stability, and KAM tori

We use the tangent-space gradient-descent algorithm introduced in Sec. II B to find periodic orbits for the kicked Ising Hamiltonian in Eq. (16). We choose an intermediate value of the coupling, J=1.09 (J=g), that puts the model in the prethermal regime (see Appendix C 1). For each bond dimension  $\chi \in [1,4]$  we run the tangent-space gradient-descent optimization of the fidelity [Eq. (12)] using over one hundred random initial conditions [66]. For small bond dimensions,  $\chi=1,2$ , we use the TDVP with a small time step dt=0.001, but for  $\chi=3,4$  for increased efficiency, we first find approximations for periodic orbits with dt=0.01 and then run a second, refining tangent-space gradient-descent optimization with a smaller TDVP time step dt=0.001, to converge to the desired precision.

From the converged instances of the tangent-space gradient descent optimization, we select instances where the optimized cost function differs from 1 by less than  $10^{-9}$ . For small bond dimensions ( $\chi = 1, 2$ ), most of the random initializations converge to such values. Notably, with increasing bond dimension, we obtain more instances converging to local minima with fidelity being significantly below one. Hence, the success rate of converging to a periodic orbit decreases with increasing bond dimension. To filter out the duplicate orbits, we analyze the fidelity between all pairs of initial points of converged periodic orbits,  $\mathcal{D}(A_L, A'_L)$  defined in Eq. (11), and identify duplicate orbits if  $\mathcal{D}(A_L, A_I) > 1 - 10^{-5}$ . Additionally, we discard near-singular orbits, where the second-largest eigenvalue of the transfer matrix  $TM(A_L, A_L)$  from Eq. (10) exceeds  $1 - 10^{-6}$ , as our algorithm assumes an injective MPS.

Periodic orbits obtained after the postprocessing procedure described above are shown in Fig. 1 for different bond dimensions. First, in Fig. 1(a) we show the expectation values of local observables  $\langle \sigma^{x,y}(t) \rangle = \langle \psi(t) | \sigma^{x,y} | \psi(t) \rangle$ , where  $\psi(t)$  is an orbit at time t in the form of the iMPS. The perfect return of the quantum wave function to itself after one period results in closed curves. Moreover, the part of the periodic evolution from Eq. (15) where the dynamics are generated by the x magnetic field results in straight segments, where  $\langle \sigma^x \rangle$  is unchanged. While the presence of entanglement is not apparent in Fig. 1(a), in Fig. 1(b) we illustrate that all orbits with  $\chi > 1$  have nonzero bipartite entanglement at all times. The relatively poor agreement between the entanglement dynamics on the orbit with the

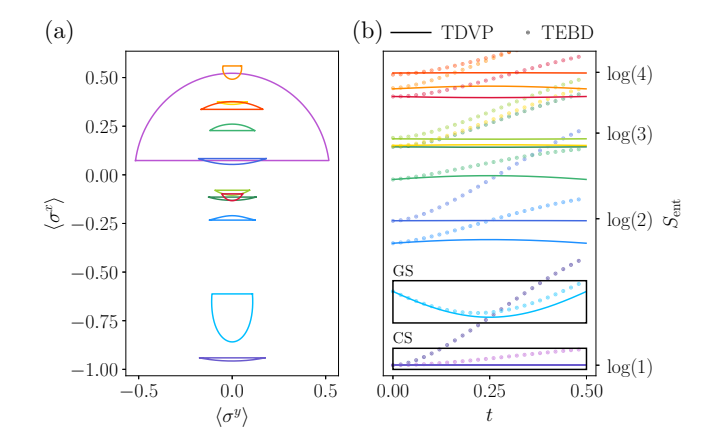


FIG. 1. (a) The dynamics of the local expectation values  $\langle \sigma^{x,y} \rangle$  along periodic orbits of different bond dimensions. Two different orbits for  $\chi=1$  are represented by violet colors, and three unique orbits for  $\chi=2$  and 4 are shown in different shades of blue and red, respectively. Finally, four orbits for  $\chi=3$  are shown in shades of green. (b) All orbits for  $\chi>1$  are characterized by nonvanishing entanglement that is a periodic function of time. Entanglement is shown only during the half-period since it is not affected by the evolution with the single-site x magnetic field during the second half-period. Dots correspond to the dynamics of entanglement in full (numerically exact) unitary dynamics obtained with time-evolving block decimation (TEBD). All orbits have been obtained for J=1.09. The two orbits in the boxes are marked as the ground state and the ceiling state (CS), the reason for which we discuss in the next section.

entanglement dynamics from exact simulations (we use time-evolving block decimation (TEBD) [22] from the ITensor [67] software package for L = 50 and cutoff =  $10^{-32}$ ) observed for most periodic obits indicates that these orbits are "high leakage." In other words, they provide a relatively poor approximation of the exact unitary dynamics. Two orbits, which we call the ground state and the ceiling state (CS) in Fig. 1 (we discuss the meaning of the names in the next section), have the smallest leakage. The high leakage of the periodic orbits obtained above may be viewed as instability with respect to the degrees of freedom outside the MPS manifold with a fixed bond dimension. We defer further investigation of leakage and its effect on the correspondence between the TDVP and full unitary dynamics until Sec. III C, and instead turn to the investigation of the stability of the orbits within a fixed- $\chi$  MPS manifold.

To study the stability of periodic orbits with respect to small perturbations in the initial state, we look at the dynamics initiated in the vicinity of the periodic orbit. Specifically, for each orbit, we perturb the initial MPS tensor randomly (by perturbing the individual tensor entries by small random values) with a perturbation of size  $\Delta = 10^{-7}$ , and visualize the resulting long-time dynamics in Fig. 2. First, we observe that the distance

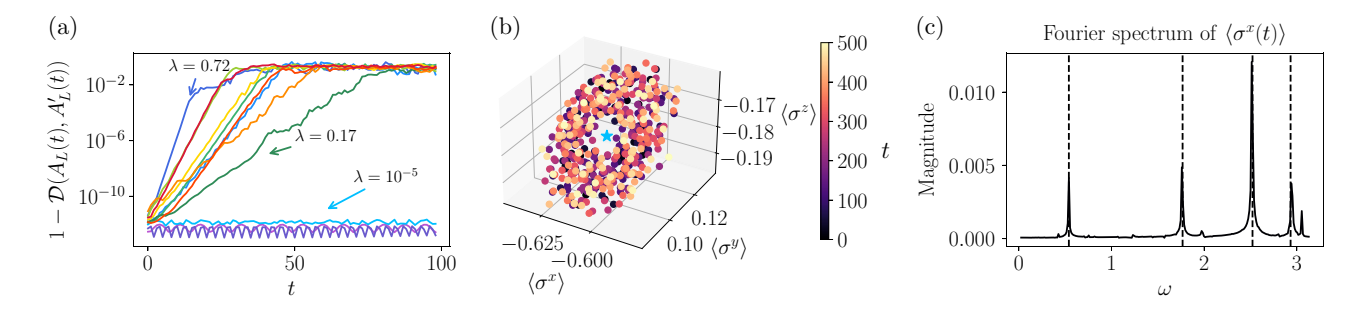


FIG. 2. (a) The distance between the time-evolved initial state on the periodic orbit and the trajectory obtained by a small deformation of the orbit, quantified by  $1 - \mathcal{D}(A_L(t), A'_L(t))$ . The trajectories and their color coding coincide with the orbits in Fig. 1 for J=1.09. Both  $\chi=1$  orbits and one of the  $\chi=2$  orbits are stable, while the remaining orbits are unstable, and small deformations lead to an exponential increase in distance with time. The Floquet exponents for the periodic orbits starting from  $\chi=2$  have the following values:  $[10^{-5}, 0.3, 0.72, 0.35, 0.17, 0.45, 0.35, 0.29, 0.35, 0.48]$ . (b) The stroboscopic dynamics of the expectation values of the local spin projections for the GS perturbed by a random perturbation with strength  $\delta=0.01$  may be understood as a projection of the KAM torus. The blue star here corresponds to the original periodic orbit values of the local observables. (c) The Fourier spectra (without the  $\omega=0$  component) of the  $\langle \sigma^x(t) \rangle$  expectation values have sharp peaks that can be interpreted as the frequencies associated with the motion on the four-dimensional KAM torus. The black dashed lines correspond to phases of the four Floquet multipliers defined in Eq. (17) that match the location of the peaks (we ignore the small peak at  $\omega\approx3.05$  as it is perturbation dependent and does not appear for all observables).

between the state on the periodic orbit and the trajectory resulting from the perturbed orbit has two qualitatively different behaviors [see Fig. 2(a)]. For most orbits, this distance shows an exponential increase with time, implying that they are unstable and can be associated with a nonzero Lyapunov exponent. However, a few orbits show robustness with respect to random perturbations, where the distance between the orbit and the perturbed state remains bounded with time, suggesting stability. The coexistence of unstable and stable orbits provides evidence for a *mixed phase space*, which has been reported earlier only for restricted MPS *Ansätze* with bond dimension  $\chi = 2$  [19].

To quantify the (in)stability of periodic orbits, we compute their Floquet multipliers, which measure how a small volume (box) around the initial point of an orbit deforms after one cycle of evolution. Since the TDVP dynamics are symplectic, the phase-space volume is preserved. As a result, the product of all Floquet multipliers is 1, reflecting the conservation of phase space volume. Mathematically, the set of Floquet multipliers,  $\Lambda$ , is defined via the eigenvalues of the Jacobian matrix resulting from the dynamics over the period of the orbit T,

$$\Lambda = \operatorname{eig} J, J_{ab} = \mathcal{T} \exp \left[ \int_0^T dt \frac{\partial \dot{A}_{L,a}}{\partial A_{L,b}} \right]_{A_L \to A_L(t)}. \quad (17)$$

Here, we have schematically denoted our dynamical variables by  $A_{L,a}$  and  $A_{L,b}$  (see the discussion below for details). For stable orbits, we expect  $|\Lambda_i| = 1$ , implying that such a box, after one period, rotates but maintains its dimensions. In this case, the eigenvalues come in complex-conjugate pairs, and the phases of  $\Lambda_i$  from each pair give the frequency of motion along the KAM torus surrounding

the orbit. In contrast, the box surrounding the unstable orbit will expand in the direction corresponding to an eigenvalue outside the unit circle,  $|\Lambda_i| > 1$ , and shrink in the direction corresponding to an eigenvalue within the unit circle,  $|\Lambda_i| < 1$ . We can also use the largest-magnitude Floquet multiplier,  $\Lambda_{\text{max}}$ , to define an effective Floquet exponent,

$$\lambda = \frac{1}{T} \ln |\Lambda_{\text{max}}|, \tag{18}$$

that loosely corresponds to the period-averaged Lyapunov exponent, akin to a finite-time or local Lyapunov exponent [68,69]. In general, we expect that the most unstable Floquet exponent has a dominant influence on the evolution of trajectories near the solution at longer times.

In the present case, where the dynamics are generated by TDVP projection onto the MPS manifold, we use a tangent space basis to remove the unphysical directions corresponding to gauge transformations and construct the Jacobian in Eq. (17) numerically (see details in Appendix B 2). Intuitively, this corresponds to indices a and b in Eq. (17) running over tangent space directions. In Fig. 2(a), we list a few values of resulting Floquet exponents  $\lambda$  [see Eq. (18)] obtained from numerical diagonalization of the Jacobian, illustrating that larger values of  $\lambda$  indeed correspond to orbits that are more unstable.

For stable orbits, in agreement with expectations, our numerical study yields small values  $\lambda \approx 10^{-5}$ , which are consistent with zero. To further gain insights into the vicinity of such stable periodic orbits, we perturb the stable orbit for  $\chi = 2$  and plot the dynamics of local spin excitation values,  $\langle \sigma^{x,y,z} \rangle$ , at stroboscopic times nT,  $n \in [1,500]$ . In

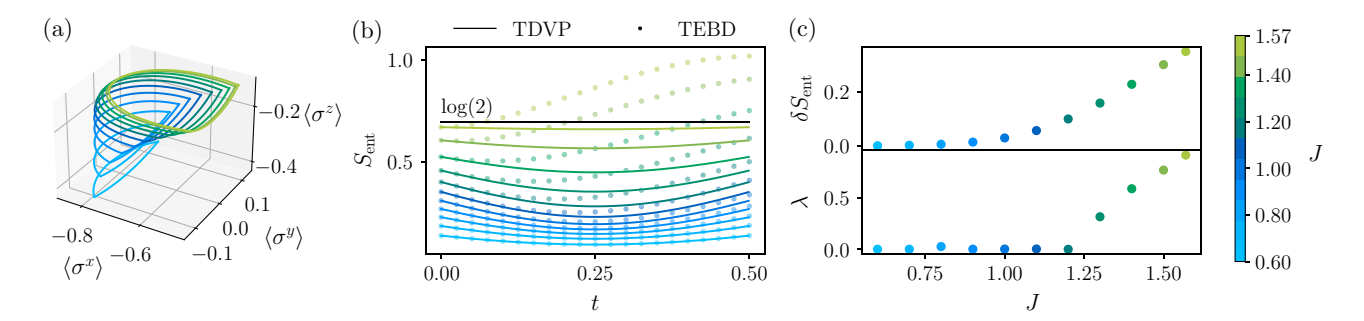


FIG. 3. (a) The smooth evolution of the low-leakage GS orbit with respect to the propagator parameter J, visualized via the dynamics of the local spin expectation values. (b) The dynamics of entanglement entropy for the first half-period of the orbit and from exact unitary dynamics for L=50 TEBD. As we increase J, the orbit moves to a more entangled region of the MPS manifold, and the leakage along the orbit increases. (c) The difference between the entanglement entropy in the exact unitary and TDVP dynamics ( $\delta S_{\rm ent}$ ) at t=T (top panel), and the corresponding Floquet exponent (bottom panel). We observe that both quantities behave in a similar way as functions of J. At  $J\approx 1.27$ , the orbit becomes unstable, and for similar values of J,  $\delta S_{\rm ent}$  starts to increase more rapidly.

Fig. 2(b), we show that these stroboscopic expectation values stay in the vicinity of the expectation value corresponding to the periodic orbit for long times. This is consistent with a mixed phase space, commonly observed in Hamiltonian dynamics [55], where stable orbits are expected to be surrounded by KAM tori [52–54]. Interpreting  $\chi^2$  nontrivial *complex* parameters of the MPS as  $\chi^2$  canonically conjugate pairs of real momenta and coordinates, we suggest that in the general case, the dimensionality of the torus is equal to  $\chi^2$ . In Fig. 2(c), we show the Fourier spectra of the observable  $\langle \sigma^x(nT) \rangle$ . The frequency peaks coincide well with the frequencies obtained from the Floquet multipliers of the stable periodic orbit, meaning that the dynamics of the observables at stroboscopic times nTis consistent with the motion on the surface of a  $\chi^2 = 4$ dimensional KAM torus. In Appendix B4, we also show evidence of a nine-dimensional torus for the stable  $\chi = 3$ periodic orbit.

# C. Deformation of orbits and their relation to eigenstates with the Ising coupling

After analyzing the set of orbits across different bond dimensions for a fixed value of the coupling, we consider the fate of the most stable  $\chi = 2$  orbit when changing the parameter J = g. The expectations from classical dynamical systems suggest that the orbit should be smoothly changing with J. This is confirmed in Fig. 3(a), which shows the smooth change in the dynamics of the local spin expectation values with  $J \in [0.6, \pi/2]$ . In Fig 3(b), we show the evolution of the entanglement dynamics for the same family of orbits. We observe that, as J changes from a small value to values close to the maximally chaotic dual-unitary point,  $J = \pi/2$ , the entanglement on the orbit approaches ln 2—the maximal value allowed by the fixed bond dimension  $\chi = 2$ . Moreover, the disagreement between the TDVP and the exact unitary dynamics increases upon increasing J.

In Fig. 3(c), we quantify the leakage of the orbit using the differences in the entanglement-entropy dynamics between the exact and TDVP evolutions and also shows the evolution of the Floquet exponent,  $\lambda$ , with the coupling. The orbit becomes unstable at  $J \approx 1.27$ , where  $\lambda$  begins to deviate from zero (see Appendix B 3, where we discuss the additional insights into this instability from the full analysis of Floquet multipliers in the complex plane). Around somewhat smaller values of the coupling J, the leakage also begins to increase more rapidly, as witnessed by the entanglement dynamics. The fact that these phenomena occur simultaneously with the entire orbit moving to more entangled regions of the  $\chi = 2$  MPS manifold highlights the potential relation between the average entanglement on the orbit, its stability, and leakage. Intuitively, we expect that orbits in nearly maximally entangled regions of a given MPS manifold, with  $S_{\text{ent}}$  approaching its strict upper bound,  $\ln \chi$ , to feature higher leakage and to typically be unstable. Indeed, in this region, the bond dimension is nearly saturated, and the MPS Ansatz cannot capture additional correlations created by unitary dynamics, giving rise to high leakage.

Additional support to this conjecture may be obtained by analyzing the effect of the periodic orbit on the exact unitary dynamics of the kicked Ising model generated by the unitary operator in Eq. (16). Specifically, we consider the inverse participation ratio (IPR) of the MPS corresponding to the initial point of the orbit,

$$I_2^{U_T} = \sum_{i=1}^{D} |\langle \psi_{\text{MPS}} | \varphi_i \rangle|^4, \tag{19}$$

defined over the complete basis of eigenstates  $\{|\varphi_i\rangle\}_{i=1}^D$  of the unitary operator, where D is the Hilbert-space dimension. The IPR quantifies how delocalized the MPS is on the basis of eigenstates, and in the case where the eigenstates

of the unitary operator are fully chaotic, the weakly entangled MPS is expected to show IPR scaling as the inverse size of the Hilbert-space dimension,  $I_2 \sim 1/D \sim e^{-sL}$ , thus decreasing exponentially with the system size.

In Fig. 4(a), we show the IPR in the basis of eigenstates for all orbits found for a fixed value of the coupling J=1.09 (see Fig. 1). Note that the Hilbert-space dimension D corresponds to the size of the translationally invariant zeromomentum sector (we do not fix the parity sector since not all orbits are parity symmetric; see Appendix B 1). While the majority of MPSs corresponding to periodic orbits show the expected exponential scaling of the IPR with L, MPSs corresponding to low-leakage  $\chi=1$  and 2 orbits in Fig. 1 have an IPR close to 1 that is slowly decreasing with L. These two states also appear to be the ground state ( $\chi=2$  low-leakage orbit) and ceiling state ( $\chi=1$  low-leakage orbit) of the effective Hamiltonian (see Appendix C), justifying their names, which were introduced earlier.

Focusing on the GS in Fig. 4(b), we show how its IPR scaling changes with the coupling J. The evolution of the IPR scaling with J should be compared to the dependence of leakage on J of the same orbit shown in Fig. 3(c). At the smallest values of J, where the orbit has very small leakage, the IPR is close to 1 and shows almost no decay with the system size, L. This implies that at small values of J, our gradient-based orbit search is capable of obtaining approximate eigenstates. From this perspective, our method bears similarity to the density matrix renormalization group (DMRG) approach [70,71] for finding ground states of local Hamiltonians. In DMRG, the MPS approximation to the ground state is obtained by minimizing the energy of the Hamiltonian, and the quality of the eigenstates can be checked by computing the variance of the Hamiltonian for the approximate MPS eigenstate. Similarly, in our case, we maximize the fidelity in Eq. (12) to find periodic orbits and check their quality via the leakage in Eq. (9). As a result, the low-leakage orbits can be interpreted as approximate eigenstates of the unitary operator generating dynamics over one period, with the dynamics on the periodic orbit corresponding to the micromotion (dynamics happening inside the period) of the driven system, with the deviation bounded by the leakage in Eq. (9).

From the above discussion, we conclude that low-leakage periodic orbits imply the existence of weakly entangled eigenstates of the unitary operator [see Eq. (16)]. Generic many-body systems are not expected to have such low-entangled eigenstates. Rather, on the contrary, all eigenstates are expected to realize an infinite-temperature ensemble [9,45–48]. However, as discussed in Sec. III A, for small coupling J, the kicked Ising model features a prethermal regime. Here, the dynamics show long-lived, quasistationary behavior before eventually thermalizing. The system effectively evolves as if governed by an

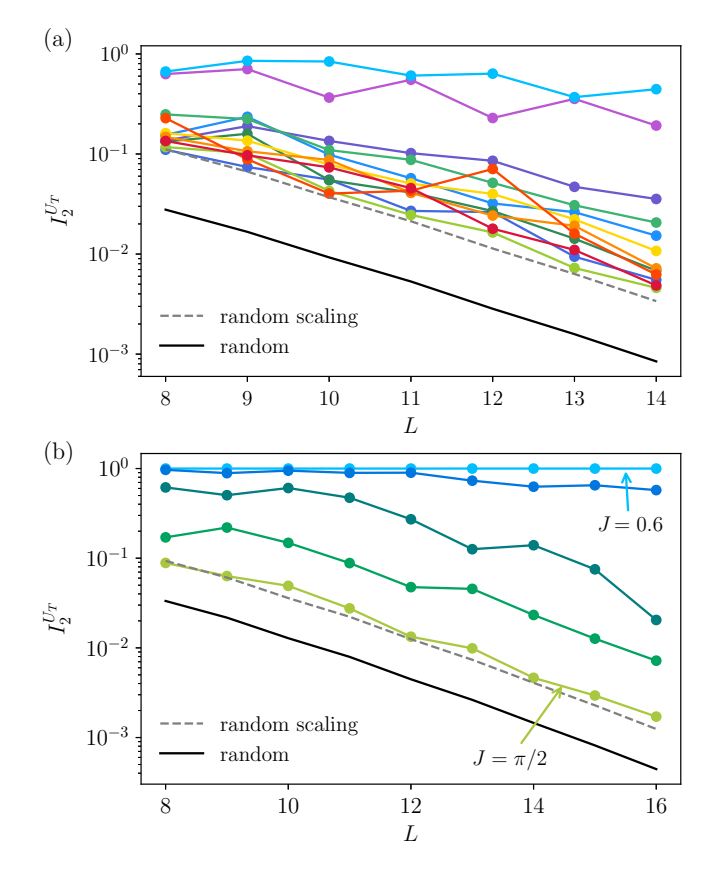


FIG. 4. (a) The inverse participation ratio (IPR) of the MPSs corresponding to periodic orbits from Fig. 1 for J=1.09 over the basis of eigenstates of the unitary from Eq. (16). For all cases, IPR decays exponentially with L, but two orbits with the lowest leakage show a parametrically slower decay of IPR. (b) The IPR scaling with L for the lowest-leakage  $\chi=2$  orbit (GS) at five different values of the coupling,  $J=0.6, 1.0, 1.2, 1.4, \pi/2$ . For J=0.6, the IPR is close to one and stays nearly constant, whereas at the dual-unitary point  $J=\pi/2$ , the IPR decays as  $\sim e^{-0.55L}$ , in agreement with expectations for a random state,  $\sim e^{-0.56L}$ . Due to MPSs being translation and inversion symmetric for this family of orbits, we consider the zero-momentum sector with parity +1.

approximately conserved effective Hamiltonian [49,50], leading to the existence of eigenstates with small entanglement. Thus, prethermal behavior explains the success in finding low-leakage periodic orbits for small J (see also Appendix C for additional details). To clarify, the prethermal behavior of eigenstates exists only in finite systems. This does not contradict our observations of stable trajectories in infinite systems, which apply to finite-time dynamics. Perfect eigenstates in infinite systems would require vanishing leakage, but, in practice, leakage is always present. Therefore, periodic trajectories do not correspond to exact eigenstates. At small system sizes, these trajectories approximate eigenstates well, but the overlap decays exponentially with system size.

## IV. DISCUSSION AND CONCLUSIONS

In this paper, we have introduced a new method for finding periodic orbits in the TDVP equations of motion projected onto the manifold of MPS for general bond dimensions. Our method maximizes the fidelity using gradient descent, therefore having complexity parametrically larger compared to the TDVP,  $O(d\chi^5)$  versus  $O(d\chi^3)$ , with the additional factor emerging due to the computation of  $\chi^2$  gradients. Applying this method to the kicked Ising model, we have found a number of periodic orbits for a range of bond dimensions  $\chi \in [1,4]$ . We have demonstrated that various techniques from classical chaos can also be applied to the variational projection of quantum dynamics. In particular, we have performed orbit stability analysis via Floquet multipliers, visualized the KAM tori surrounding the stable orbits, and characterized the dimension of KAM tori via Fourier transforms of time series of local observables.

By adjusting the Ising coupling, we have tuned the quantum dynamics between prethermal and chaotic regimes. At the same time, we have tracked the fate of periodic orbits and observed their smooth deformation and the onset of instability upon approaching the maximally chaotic point. In the prethermal regime, our method for finding orbits results in approximate eigenstates of the unitary operator generating the exact dynamics over one period and, thus, may be viewed as a generalization of the DRMG to the periodically driven setting. In the chaotic regime, we observe that although periodic orbits survive, they become unstable and no longer correspond to approximate eigenstates. It remains to be seen if they still leave imprints on quantum dynamics, despite their high leakage.

The TDVP projection of quantum dynamics onto the MPS manifold is known to result in a classical dynamical system with a symplectic structure. Yet, the resulting classical dynamics have not been studied in detail until now. with the exception of a few works that have analyzed the spectrum of Lyapunov exponents resulting from long-time dynamics [29] and analytically studied TDVP projection for a special class of MPSs with a small number of parameters [19,30]. The main achievement of the present work is the demonstration that such dynamics, despite the complex nature of dynamical variables, can be systematically studied with tools from classical chaos. The key insight, consistent with the general approach to MPS [57], is to consider only gauge-invariant quantities, such as fidelity and local observables, and use these to infer the properties of the classical dynamical system, while never unpacking the dynamical variables, leaving them hidden inside MPS tensors.

The possibility of obtaining the classical limit of quantum dynamics with TDVP projection onto the MPS manifold opens a number of exciting directions. First, a practical application of our algorithm is the systematic

search for nonthermal eigenstates that may appear at high energy densities in Hamiltonian systems and are known as quantum many-body scars [72–77] (Corresponding results are discussed in Appendix D.). The appearance of scars has been linked to MPS periodic orbits with sufficiently slow entanglement growth (small leakage) [19,30], and to unstable orbits in the semiclassical description of many-body quantum systems [78–82]. We note that the MPS-based approach also includes a naive semiclassical limit (dynamic mean field) for the smallest bond dimension  $\chi = 1$ , but can also systematically go beyond the dynamical mean field by including additional degrees of freedom describing correlations (equivalently, entanglement). This is also potentially possible in dynamical mean-field approaches, by including fluctuations around the trajectories, but for local spin-1/2 degrees of freedom, such an approach is a priori not well controlled. In contrast, MPSs are guaranteed to capture the dynamics up to times that are logarithmic in the bond dimension [61,62]. Moreover, by finding MPS periodic orbits in regions characterized by small leakage, it may be possible to observe quantum signatures of phenomena established in classical dynamical systems, such as bifurcation transitions in the periodic orbits, Arnold diffusion [83,84], and others.

The dynamics of other classes of quantum systems that avoid thermalization are another attractive avenue for the application of our method. In particular, a straightforward extension of our algorithm to finite-size MPS simulations without translational invariance will open the door to the study of the kicked Ising model with disorder—one of the models realizing Floquet many-body localization [45,85–88]. It would be interesting to check if the present algorithm is capable of finding eigenstates within the Floquet many-body localized phase for system sizes beyond those that can be reached with exact diagonalization. It also remains to be understood whether the classical phase portraits in the many-body localized phase feature large regular regions of the phase space, thereby directly establishing an analogy between many-body localization and the Kolmogorov-Arnold-Moser theorem [89]. In a different direction, the study of similar questions for Bethe-Ansatz integrable models [90] with translational invariance is also an attractive avenue. For such models, however, additional research is needed, as it may require the nontrivial extension of the TDVP that is potentially capable of preserving additional conservation laws.

Finally, we expect that our approach may also provide useful insights for chaotic, periodically driven, or Hamiltonian systems. In particular, we conjecture that in a chaotic regime of quantum dynamics, periodic orbits are hidden in the regions with nearly maximal entanglement allowed by the MPS manifold and are generally unstable. It remains to be understood if the properties of such orbits can nevertheless provide useful insights into quantum thermalization.

Note added. We have recently become aware of a related study by Ren et al. [91], where a method based on an iterative sequence of finite time evolution and projection back onto an MPS manifold has been developed to identify periodic orbits related to quantum many-body scars.

## **ACKNOWLEDGMENTS**

We acknowledge useful discussions with C. Kollath, A. Green, and D. Huse. E.P., M.L., and M.S. acknowledge support by the European Research Council under the European Union's Horizon 2020 research and innovation program (Grant Agreement No. 850899). This research was funded in whole or in part by the Austrian Science Fund (FWF) (Grant No. 10.55776/COE1). For open access purposes, the author has applied a CC BY public copyright license to any author accepted manuscript version arising from this submission. M.L. acknowledges support by the Deutsche Forschungsgemeinschaft (DFG, German Research Foundation) under Germany's Excellence Strategy—EXC-2111—390814868. This research was supported in part by National Science Foundation (NSF) Grant No. PHY-2309135 to the Kavli Institute for Theoretical Physics (KITP) and by the Erwin Schrödinger International Institute for Mathematics and Physics (ESI).

#### DATA AVAILABILITY

The data and the source code that support the findings of this paper are openly available [92].

# APPENDIX A: IMPLEMENTATION OF TDVP AND GRADIENT DESCENT

In this appendix, we discuss the construction of the mixed gauge of the iMPS, the iMPS tangent bases, and the TDVP algorithm that we implement in our work based on Refs. [57,58]. After this, we provide the details for the implementation of the gradient-descent algorithm introduced in Sec. II B for the search for closed orbits.

#### 1. Mixed-canonical form

The first step in numerical algorithms dealing with the iMPS is to obtain the mixed-canonical form, which fixes part of the gauge freedom, as shown in Eq. (3). The algorithm implemented in our code follows the approach described in Ref. [57], which we briefly review here for completeness.

The concept of gauge fixing arises from the observation that, given an MPS representation as in Eq. (2), the tensor A can be transformed via an invertible matrix X according to the rule  $A_{ij}^{\prime s} = X_{im}^{-1} A_{mn}^s X_{nj}$  (throughout the following, we denote such a transformation compactly as  $X^{-1}AX$  unless otherwise specified). Importantly, this transformation leaves the physical state invariant. This gauge freedom allows us to impose additional structure on the MPS. In

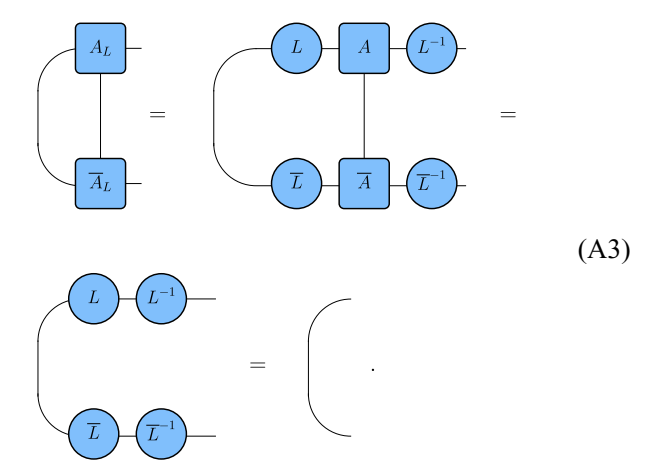
particular, it enables us to choose a transformation X that brings the tensors into a form satisfying either the left or right orthonormalization condition,

therefore, partially fixing the gauge.

In this section, we use the following notation. To find the left-canonical form, we call such a transformation L, and so have  $A_L = LAL^{-1}$ , and analogously for the right-canonical form, we call the transformation R. The matrix L can be found from the left fixed point of the transfer matrix TM(A,A),

$$\begin{array}{c}
A \\
\hline
I \\
\hline
A
\end{array} = 
\begin{array}{c}
I \\
\hline
A
\end{array} ,$$
(A2)

by solving the equation  $l = L^{\dagger}L$  for L. Then the left gauge-fixing condition is satisfied as



The same procedure can be applied to the right-canonical form. After finding  $A_L$  and  $A_R$ , the only degrees of freedom that are left are unitary transformations,

$$A'_{L} = U^{\dagger} A_{L} U,$$

$$A'_{R} = V^{\dagger} A_{R} V,$$
(A4)

which leave the tensors left or right orthonormal.

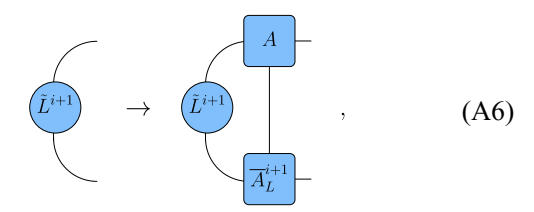
The procedure for obtaining the left- and right-canonical forms of an MPS tensor can be formulated as an iterative process. Given a tensor A, our goal is to find a transformation matrix L such that the transformed tensor  $A_L = LAL^{-1}$  satisfies the left gauge-fixing condition in Eq. (A3). The optimal way to find  $A_L$  is to solve  $LA = A_LL$ . The iterative

algorithm for that proceeds as follows. Starting from an initial guess  $L^i$ , we compute the product  $L^iA$  and perform a QR decomposition (a decomposition of a matrix into a product of an orthonormal matrix Q and an upper triangular matrix R) on the result. This yields a new tensor  $A_L^{i+1}$  and an updated matrix  $L^{i+1}$  as

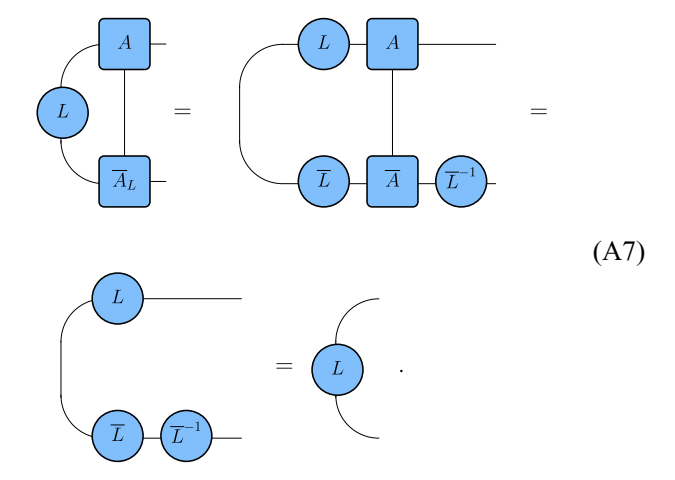
$$-L^{i} - A - = -A_{L}^{i+1} - L^{i+1} - . \tag{A5}$$

The updated matrix is then used as the input for the next iteration, and the process is repeated until convergence.

The QR decomposition is unique up to the signs inside the decomposition. That is why we fix the diagonal elements of the triangular matrix to be positive. The algorithm reaches a fixed point when  $L^{(i+1)} = L^{(i)} = L$ , and the resulting tensor  $A_L$  is left-orthonormal by construction. To accelerate convergence, once an intermediate  $A_L^{i+1}$  has been found, we improve the next guess for L by replacing it with a refined fixed point  $\tilde{L}^{i+1}$  of the map,



as the following is satisfied for the left-canonical form:



The general procedure described above is summarized in Algorithm 1. For the eigensolver, we have used the KrylovKit software package in JULIA and the LAPACK library in C++, with a convergence tolerance set to  $10^{-15}$ .

The procedure for obtaining the right-canonical form mirrors that of the left one. However, instead of starting with the original tensor A, we begin with the left-canonical tensor  $A_L$ . In this case, we perform an RQ decomposition (a decomposition of a matrix into a product of an upper triangular matrix R and an orthonormal matrix Q) to extract the right-canonical form. The central site C is obtained from R, which we have after right orthonormalization by

#### ALGORITHM 1. Left orthonormal form.

```
Require: A, L, \eta
 1: \hat{L} = L/\|L\|
 2: L_{\text{old}} = L
 3: (A_L, L) = \mathsf{QRGauged}(LA) \triangleright Gauged \ QR \ decomposition
                                      Eq. (A5)
 4: L = L/\|L\|
 5: \delta = \|\hat{L} - \hat{L}_{\text{old}}\|
 6: while \delta > \eta do
          L = \mathtt{eigensolver}(X 	o \mathrm{TM}(X), L, \delta/10) \triangleright \mathit{Finding fixed}
                           point of transfer map in Eq. (A6)
          L = \mathtt{QRGauged}(L)
 8:
          L = L/||L||
 9:
          L_{\text{old}} = \ddot{L}
10:
11:
          (A_L, L) \leftarrow \mathsf{QRGauged}(LA) \triangleright Gauged \ QR \ decomposition
                                            Eq. (A5)
12:
          L = L/||L||
          \delta = \|L - L_{\rm old}\|
13:
14: return A_L, L
```

doing gauged singular-value decomposition (SVD) on it and transforming  $A_L$  and  $A_R$  through U and V matrices as in Eq. (A4). We also do gauge fixing in SVD, as the phases of singular vectors have a phase freedom. For that, we scan through left-singular vectors and make the first nonzero component real and positive, adjusting the phase of the right-singular vectors accordingly. The entire procedure for obtaining the mixed-canonical form is summarized in Algorithm 2.

We note that the iterative procedure described above may encounter an issue when initialized with an MPS that has a poorly conditioned entanglement spectrum. Intuitively, this corresponds to an initialization with a state of a nominal bond dimension  $\chi$ , which is nearly identical to the state with a smaller bond dimension  $\chi' < \chi$ . For such initializations, the procedure of computing  $A_R$  was stuck in an infinite loop as R does not converge. Intuitively, the presence of very small singular values in the entanglement spectrum leads to the matrix R having small values on the diagonal, which does not allow fixing the gauge correctly in the OR decomposition. This could be partially fixed by restarting the algorithm, using a different initial guess of R. However, in cases when several such restarts do not help, we terminate the entire procedure of searching for the closed orbit and use a different initial guess, as the orbit in question can most likely be identified using a smaller bond dimension.

# ALGORITHM 2. Find mixed gauge $\{A_L, A_R, C\}$ .

```
Require: A, \eta

1: (A_L, \sim) = \text{LeftOrthonormalize}(A, L_0, \eta)

2: (A_R, C) = \text{RightOrthonormalize}(A_L, C_0, \eta)

3: (U, C, V) = \text{SVDGauged}(C)

4: A_L = U^{\dagger} A_L U

5: A_R = V^{\dagger} A_R V

6: return A_L, A_R, C
```

## 2. Tangent basis and TDVP realization

We start with the construction of the tangent basis for the iMPS in the mixed-canonical gauge. The tangent space for the iMPS is defined as the set of all possible infinitesimal changes of the iMPS that correspond to physical changes of the quantum state. The most general form of the tangent vector has the following form:

$$|\Phi(V, A_L, A_R)\rangle = \sum_{n} \dots - \underbrace{A_L}_{S_{n-1}} \underbrace{A_L}_{S_n} \underbrace{V}_{S_{n+1}} \underbrace{A_R}_{S_{n+1}} - \dots, \quad (A8)$$

where tensor V parametrizes directions in the tangent space. In this form, tangent vectors also have a gauge freedom. Changing  $V \rightarrow V + A_L B - B A_R$  for any matrix B leaves the tangent vector the same. We could fix this freedom by implementing left gauge fixing:

$$\begin{array}{c}
V \\
\hline
\overline{A_L}
\end{array} = 0.$$
(A9)

Following the above equation, we construct the tensor V using the null space of the tensor  $A_L$  with merged left bond and physical indices, denoted as v, which is a  $d\chi \times (d-1)\chi$  matrix, where the number of columns corresponds to the size of the null space of the tensor  $A_L$ :

$$= 0, \qquad = 0.$$
 (A10)

Having matrix  $\nu$  we define unique tangent-space directions using a set of  $(d-1)\chi \times \chi$  dimensional tensors  $\{X^{(\alpha)}\}$  as follows:

$$-V^{(\alpha)} - = -V - X^{(\alpha)} - . \tag{A11}$$

To construct an orthogonal tangent basis, we choose  $\{X^{(\alpha)}\}$  as the basis in the space of complex matrices of size  $(d-1)\chi \times \chi$ . Each matrix  $X_{\text{re(im)}}^{(\alpha)}$  in the set has exactly one nonzero element 1(i). This choice provides  $2(d-1)\chi^2$  independent basis vectors, where the factor of 2 arises from treating real and imaginary parts as separate components. Equation (A11) defines the tangent basis as two sets of tensors  $\{V_{\text{re}}^{(\alpha)}\}$  and  $\{V_{\text{im}}^{(\alpha)}\}$ , which satisfy the relation

$$iV_{\rm re}^{(\alpha)} = V_{\rm im}^{(\alpha)},\tag{A12}$$

where index  $\alpha$  runs over  $\alpha \in [1, (d-1)\chi^2]$ .

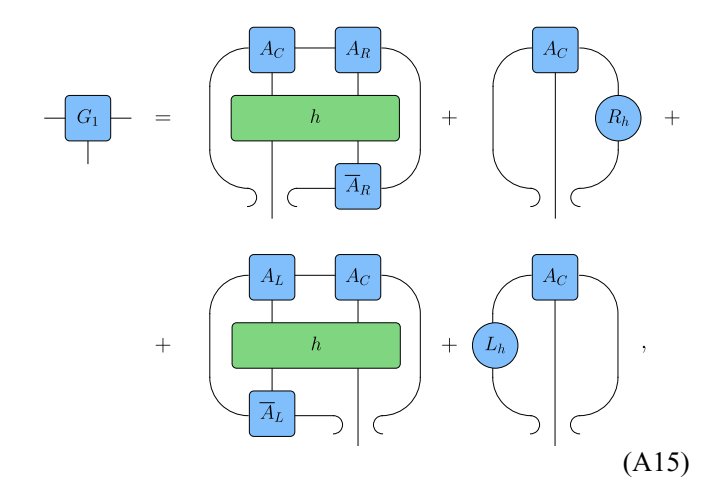
The tangent space of the iMPS plays the main role in TDVP realization. The TDVP equation of motion is a projected Schrödinger equation:

$$\partial_t |\psi(A_L, A_C, A_R)\rangle = -i\mathcal{P}H|\psi(A_L, A_C, A_R)\rangle.$$
 (A13)

The projector in the TDVP equation maps the action of the Hamiltonian back onto the tangent space spanned by the basis in Eq. (A12). The most optimal way to project the dynamics on the manifold is to minimize the leakage or the distance between the projected vector and the derivative vector, and the exact form of such a projector can be found in Ref. [57]. Due to its structure, Eq. (A13) splits into two equations, one being for tensor  $A_C$ , and the other for C:

$$\dot{A}_C = -iG_1(A_C), 
\dot{C} = iG_2(C).$$
(A14)

Here,  $G_1$  and  $G_2$  are linear Hermitian maps that take the tensor  $A_C/C$  and return a tensor with the same dimensions. They represent the action of the projected Hamiltonian on the MPS. The solution of Eq. (A14) can be schematically represented as an exponential of these maps  $A_C(t) = e^{-iG_1t}A_C(0)$  and  $C(t) = e^{iG_1t}C(0)$ . The equations below show the action of  $G_1$  and  $G_2$  on tensors  $A_C$  and C:



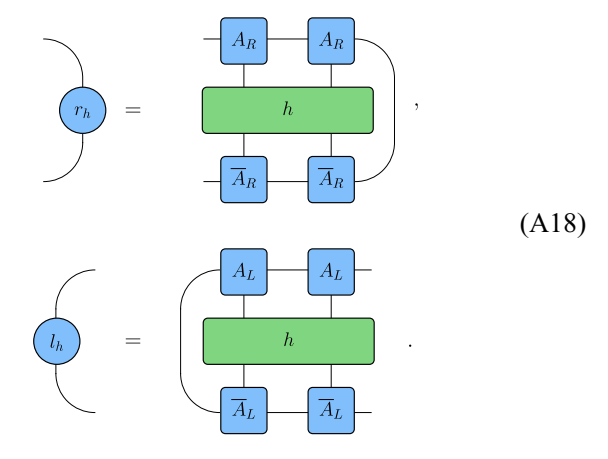
$$-\underline{G_2} - = \overline{A_L}, \qquad (A16)$$

where in Eq. (A16) dependence on C is coming from the relation  $(A_L)_{ij}^s C_{jk} = (A_C)_{ik}^s$ .

In Eqs. (A15) and (A16),  $(L_h|$  and  $|R_h)$  are the environments on the left and on the right, which represent the case when the Hamiltonian acts to the left side from the updating site and to the right side from the updating

site. Equation (A17) shows the left environment tensor construction:

where  $l_h(r_h)$  is defined as



The series in Eq. (A17) and in the analogous equation for  $R_h$ , could be rewritten in the following form:

$$(L_h| = (l_h| \sum_{0}^{\infty} TM(A_L, A_L)^k,$$

$$|R_h| = \sum_{0}^{\infty} TM(A_R, A_R)^k | r_h).$$
(A19)

To find the left and right environments, one needs to sum an infinite number of transfer matrices  $TM(A_{L/R}, A_{L/R})$  as in Eq. (A17). Let us now concentrate on the  $(L_h|$  vector for simplicity. The transfer matrix  $TM(A_L, A_L)$  has a dominant eigenvalue of unit magnitude, with corresponding left and right eigenvectors denoted by (1| and |R), respectively. The projection  $(l_h|TM(A_L, A_L)^k|R) = (l_h|R)$  represents the energy-density expectation value that does not depend on the position of Hamiltonian k. The same logic applies to  $|R_h|$ . Then, to find the right and left environments in Eq. (A19) we solve two equations:

$$(L_h | [\mathbb{1} + |R)(\mathbb{1} | - TM(A_L, A_L)] = (l_h | - (l_h | R)(\mathbb{1} |, [\mathbb{1} + |\mathbb{1})(L| - TM(A_R, A_R)] | R_h) = |r_h) - |\mathbb{1})(L|r_h).$$
(A20)

At this point, we have all the building blocks to perform time evolution by one time step. According to Eq. (A14),  $A_C(\delta t) = e^{-iG_1\delta t}A_C(0)$  and  $C(\delta t) = e^{iG_2\delta t}C(0)$ . After applying time evolution for time  $\delta t$  and obtaining tensors  $A_C(\delta t)$  and  $C(\delta t)$ , we have to extract  $A_L(\delta t)$  and  $A_R(\delta t)$ . For this, we join two indices of  $A_C$  to the right (upper index r) or the left (upper index l) and apply a polar decomposition:

$$A_C^l = U_{AC}^l P_{AC}^l, \quad A_C^r = P_{AC}^r U_{AC}^r,$$
 (A21)

$$C = U_C^l P_C^l, \quad C = P_C^r U_C^r. \tag{A22}$$

Then, the tensors  $A_L$  and  $A_R$  are obtained as follows:

$$A_L = U_{A_C}^l U_C^{l\dagger}, \quad A_R = U_C^{l\dagger} U_{A_C}^r. \tag{A23}$$

Above, we have discussed how to evolve the MPS tensors  $A_{L/C/R}/C$  of the system by one time step. Let us now move to the integration procedure for the entire MPS. To better understand the integration of the TDVP equation for infinite MPSs, let us first look at the general finite-systemsize MPSs. To propagate the finite system, the following steps are needed. Consider all  $A_L(n-1)$  to the left of n as already evolved by one step, and  $A_R(n+1)$  and further not. For systems without translation invariance, all tensors are different, and so the tangent spaces, projectors, and maps  $G_{1,2}$  are likewise different. The procedure is the following:

- (a) Evolve the central tensor according to Eq. (A14):  $\tilde{A}_C(n) = e^{-iG_1(n)\delta t}A_C(n)$ .
- (b) Do QR decomposition to extract  $A_L$  and C:  $\tilde{A}_C(n) = \tilde{A}_L(n)\tilde{C}(n)$ .
- (c) Evolve tensor C according to Eq. (A14):  $\hat{C}(n) = e^{iG_2(n)\delta t}\tilde{C}(n)$ .
- (d) Absorb the new  $\hat{C}$  to  $A_C(n+1) = \hat{C}(n)A_R(n+1)$  and continue to the next site.

For an infinite system, integration works somewhat differently. Compared to the above procedure, the iMPS should remain translationally invariant for all times t. This implies that we should apply the procedure above until  $A_C(n) = A_C(n+1)$ . Another way to look at this relation is to note that after the propagation for one time step, we obtain the same matrix C with which we started,  $C(t+\delta t) = C(t)$ . We can use this to find  $\tilde{C}$  as a *backward evolution* of C, because  $\hat{C} = C = e^{iG_2\delta t}\tilde{C}$ . Then we have  $\tilde{C} = e^{-iG_2\delta t}C$ . And finally, from  $\tilde{A}_C$  and  $\tilde{C}$  we can obtain  $\tilde{A}_L$  and  $\tilde{A}_R$ . Thus, the time-evolution procedure for the iMPS can be summarized by the following steps:

- (a) Time evolve the center-site tensor forward in time:  $\tilde{A}_C = e^{-iG_1\delta t}A_C$ .
- (b) Time evolve the center-site tensor backward in time:  $\tilde{C} = e^{-iG_2\delta t}C$ .
- (c) Find and update  $\tilde{A}_L$ ,  $\tilde{A}_R$  from  $\tilde{A}_C$  and  $\tilde{C}$  according to Eq. (A23).

#### ALGORITHM 3. Iterator for gradient-descent optimization.

```
 \begin{aligned} & \textbf{Require: } parameters, \, c \\ & 1: \, \textbf{Construct } A \, \textbf{from } parameters \\ & 2: \, (A_L, \sim, \sim) = \texttt{MixedCanonical}(A) \\ & 3: \, (A_{Lnew}, c) = \texttt{GradientDescent}(A_L, c) \\ & 4: \, \quad \textbf{while } (F(A_{Lnew}) - F(A_L)) > tol \mid\mid (1 - F(A_{Lnew})) > atol \\ & \textbf{do} \qquad \qquad \triangleright F \, \textit{from Eq. (12)} \\ & 5: \, \quad | A_L = A_{Lnew} \\ & 6: \, \quad (A_{Lnew}, c) = \texttt{GradientDescent}(A_L, c) \\ & 7: \, \quad | c = \min(c, max_c) \\ & 8: \, \textbf{return } A_{Lnew} \end{aligned}
```

# 3. Gradient-descent algorithm and convergence properties

To run the algorithm, we initialize a random MPS by generating a vector of  $2d\chi^2$  random numbers in the range [-1,1] and reshaping it to a complex matrix A of size  $\chi \times d \times \chi$ , which we use to start the optimization. First, we construct the left-canonical form and then proceed with the gradient-descent optimization of the cost function. The conceptual description of the iterator of the algorithm and initial preparation are combined in Algorithm 3.

This procedure relies on a tangent-space gradient-descent subroutine, which is briefly described in Sec. II B. Here, we provide a more detailed description of this procedure, summarized in Algorithm 4. First, we compute gradients using a tangent-space basis. These gradients are then used to construct the update tensor  $\delta A_L$ , which determines the direction of the update. To ensure effective optimization, the learning rate, denoted by c, is adjusted as described in Sec. II B, and this adjusted rate is applied to update the tensor  $A_L$ .

The convergence of the algorithm for a random initialization is illustrated in Fig. 5. As the algorithm converges, the improvement in fidelity at each iteration decreases until it reaches machine precision, at which point the

## ALGORITHM 4. Gradient descent.

```
Require: A_L, c
 1: g_{\rm re/im}^{\alpha} = \frac{F(A_L + \Delta V_{\rm re/im}^{(\alpha)}) - F(A_L - \Delta V_{\rm re/im}^{(\alpha)})}{\alpha}
 2: \delta A_L = \sum_{\alpha} (g_{\rm re}^{\alpha} + ig_{\rm im}^{\alpha}) V_{\rm re}^{(\alpha)}
                                                      \triangleright Using \mathcal{D}(A, A) from Eq. (11)
 3: Normalize \delta A_L
 4: A_{Lnew} = A_L + c\delta A_L
 5: f = F(A_{Lnew})
                                                                          \triangleright F from Eq. (12)
 6: if f > F(A_L) then
         c = c * \xi
     while f \leq F(A_L) do
           c = c/\tau
           A_{Lnew} = A_L + c\delta A_L
10:
           f = F(A_{Lnew})
11:
           if c < \epsilon then
12:
           break
14: Normalize A_{Lnew}
                                                      \triangleright Using \mathcal{D}(A, A) from Eq. (11)
15: return A_{Lnew}, c
```

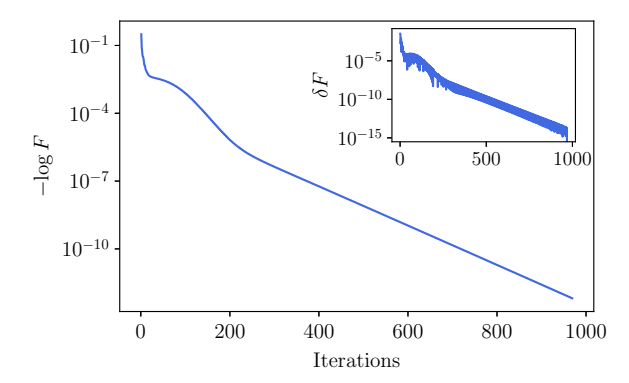


FIG. 5. The performance of the gradient-descent algorithm using the tangent space of the iMPS. The algorithm terminates when  $\delta F$  reaches  $10^{-15}$ . The data are for the GS orbit from Fig. 1.

process terminates. For our search, we set the absolute tolerance (ato1) and the tolerance (to1) to  $10^{-15}$ , with the maximal learning rate  $\max_c = 1$ , and parameter  $\xi = 1.2$  ( $\tau = 1.4$ ) controlling the dynamical updates decreasing (increasing) the learning rate. The finite difference used to calculate gradients is set to  $\Delta = 10^{-5}$ , and the learning rate at which the procedure halts is chosen as  $\epsilon = 10^{-14}$ . The initial value of the learning rate  $\epsilon$  is chosen as 0.1. These parameters have been selected to ensure both accuracy and computational efficiency.

Similar to the procedure for finding the canonical form (see the comment at the end of Appendix A 1), the gradient-descent algorithm also faces a problem when converging to the state that corresponds to a lower bond dimension  $\chi' < \chi$  compared to the fixed bond dimension  $\chi$ . For such instances, we observe that the number of nonzero directions in the tangent space decreases from  $2\chi^2$  to  $2\chi'^2$  at a certain point. We observe that this causes the gradient vector to be ill behaved: the change of nonzero components of the gradient is very rapid (the second derivative is very large), causing the learning rate of the gradient descent to shrink and leading to the eventual halting of the optimization.

# APPENDIX B: CLASSICAL PROPERTIES OF THE PERIODIC ORBITS

In this appendix, we discuss the classical properties of the periodic orbits. First, we analyze the inversion symmetry. Next, we explain the construction of the Jacobian using a tangent-space basis that is required for the study of classical stability of periodic orbits. Using the spectrum of the Jacobian, we also provide details for the onset of stability of the periodic orbit studied in Sec. III C. After that, we demonstrate the stable periodic orbit for  $\chi=3$ , analyze the Fourier spectra of the correlation functions, and reveal a nine-dimensional KAM torus. Finally, we compare periodic orbits found for different values of the bond dimension.

## 1. Inversion symmetry of periodic orbits

The kicked Ising model has spatial inversion symmetry, often referred to as parity. However, our algorithm for finding periodic orbits does not impose this symmetry, and we do not restrict our initial guess to having inversion symmetry. Hence, we expect that the orbit search may find both inversion-symmetric and inversion-breaking orbits. Indeed, from the 12 orbits that we discuss in Sec. III B, three orbits are not inversion symmetric. Since the Hamiltonian is inversion symmetric, all inversion-breaking orbits have a partner periodic orbit that can be obtained via the action of spatial inversion.

An example of such a periodic orbit is illustrated in Fig. 6, where we use the expectation values of Pauli matrices on adjacent sites to demonstrate the absence of inversion symmetry. The same figure also shows expectation values for the spatially inverted orbit. This orbit is obtained by transposing the bond indices of the MPS tensor  $A_L(0)$ , which correspond to the reflection of spatial coordinates. Such transposed MPSs correspond to different periodic orbits, as shown in Fig. 6.

While the occurrence of classical periodic orbits with a lower symmetry compared to the Hamiltonian is natural, it prompts the discussion of the correspondence between low-leakage periodic orbits and eigenstates of the unitary operator generating dynamics over one period,  $U_T$ . The eigenstates of  $U_T$  are expected to obey the same symmetries as the Hamiltonian. Hence, they cannot correspond to inversion-breaking periodic orbits. However, using the fact that each inversion-breaking periodic orbit has a partner with the same period, we can try to form inversion-symmetric and antisymmetric periodic orbits. Notably, these combinations will correspond to a noninjective MPS

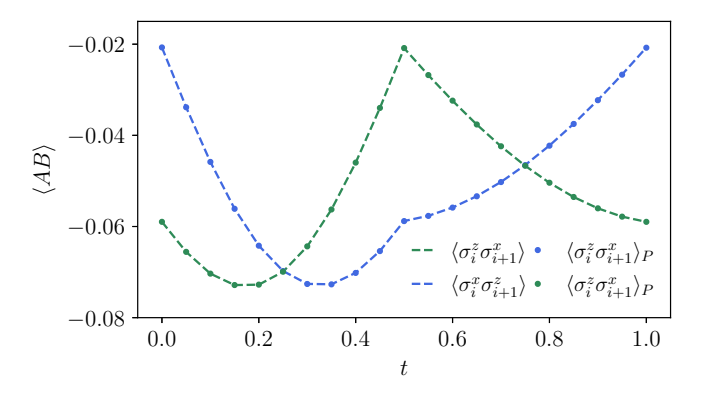


FIG. 6. An example of a periodic orbit without inversion symmetry (Fig. 1  $\chi=3$  green line, sixth from the bottom). The absence of inversion symmetry is manifest in the correlation functions of the Pauli operators for adjacent sites,  $\langle \sigma_i^z \sigma_{i+1}^x \rangle \neq \langle \sigma_i^x \sigma_{i+1}^z \rangle$  shown by dashed green and blue lines. Correlation functions calculated for the spatially inverted periodic orbit (see description in the text) are denoted as  $\langle ... \rangle_P$  and are shown by dotted lines.

representation with a larger bond dimension [as a sum or difference of two will have a transfer matrix with two eigenvalues with magnitude 1, similar to the Greenberger-Horne-Zeilinger (GHZ) state], which are beyond the applicability of our algorithm. It remains to be seen if the intrinsic nonlinearity introduced by the projection for non-injective MPS may still allow such linear combinations of periodic orbits to remain periodic orbits. In any case, we speculate that the presence of low-leakage inversion-breaking orbits may indicate a tendency to spontaneous inversion symmetry breaking.

## 2. Algorithm for the calculation of the Jacobian

To construct the Jacobian, we use a tangent-space basis,  $\{V\} = \{V_{\rm re}, V_{\rm im}\}$ , as it encodes all physical directions corresponding to changes in the quantum state. We first take an initial state corresponding to the periodic orbit at time t=0,  $A_L(0)$ , and perturb it with strength  $\Delta$  along a particular tangent-space direction,  $V^{(i)}$ . After evolving the perturbed state for one period using the TDVP, we expand the resulting state,  $A_L^{\rm pert}(T)$ , over the tangent basis at the same point  $A_L(0)$ . Computing the expansion of  $A_L^{\rm pert}(T)$  over the basis  $\{V\}$ , we face the problem of the gauge freedom of the MPS. The tangent basis is very sensitive to the gauge. This is why, if during the evolution the state changes gauge, the difference between  $A_L^{\rm pert}(T)$  and  $A_L(0)$  cannot be expanded over the tangent-space basis of  $A_L(0)$ .

In order to avoid dealing with gauge fixing, we rely on the same notion of distance between states [Eq. (11)] as used for the search for periodic orbits. Specifically, we choose  $\{\beta_i\}$  as a set of parameters for the optimization and construct the tensor  $\tilde{A}_L^{\text{pert}} = A_L(0) + \beta_i V^{(i)}$ , and normalize it. Then, we maximize the fidelity  $\mathcal{D}(A_L^{\text{pert}}(T), \tilde{A}_L^{\text{pert}})$  over the parameters  $\{\beta_i\}$  using the OPTIM software package in JULIA and taking into account that  $\tilde{A}_L^{\text{pert}}$  should be always normalized. Effectively, this optimization finds the expansion of the perturbation at time T over the tangent-space basis using a gauge-invariant cost function. The resulting coefficients  $\{\beta_i\}$  should then be divided by  $\Delta$  to obtain the finite-difference approximation of the given matrix element of the Jacobian (see the expression in Algorithm 5).

The Jacobian constructed according to Algorithm 5 is influenced by several sources of numerical errors. First, we use a finite-difference approximation for the derivatives. For our computations, we choose  $\Delta=10^{-3}$  as we have observed that taking smaller values has little effect on the Jacobian matrix. The second source of numerical errors comes from the fact that orbits may not be perfectly periodic due to the imperfect convergence of the gradient-descent algorithm. Finally, the third source of errors could potentially come from the numerical maximization of the fidelity  $\mathcal{D}(A_L^{\text{pert}}(T), \tilde{A}_L^{\text{pert}})$ . At this point, we encounter the problem of when the optimization algorithm selects the

#### ALGORITHM 5. Jacobian construction.

```
 \begin{aligned} & \textbf{Require:} \ A_L(0), \left\{V\right\} \\ & 1: \ \textbf{for} \ i \in [1, 2\chi^2] \ \textbf{do} \\ & 2: \ | \ A_L^{\text{pert}}(0) = A_L(0) + \Delta V^{(i)} \\ & 3: \ | \ \text{Normalize} \ A_L^{\text{pert}}(0) \\ & 4: \ | \ A_L^{\text{pert}}(T) = U_T(A_L^{\text{pert}}(0)) \\ & 5: \ | \ \text{Introduce parameters} \ \left\{\beta_j\right\} \ \text{and tensor} \\ & A_L^{\text{pert}} = A_L(0) + \beta_i V^{(i)} \\ & 6: \ | \ \beta_j = \max_{\left\{\beta\right\}} \left(g(A_L^{\text{pert}}(T), \tilde{A}_L^{\text{pert}})\right) \\ & 7: \ | \ Jac_{i,j} = \beta_j/\Delta \end{aligned}
```

correct direction in the space of parameters  $\beta$  but results in a slightly larger magnitude of coefficients, as we normalize  $\tilde{A}_L^{\mathrm{pert}}$  every time we construct it. Normalization is required to compare two MPSs according to Eq. (11). To avoid this issue, we choose a zero vector as an initial guess for the optimization. In this case, we expect to fall into the local minima near  $A_L(0)$ . Finally, we expect that the finite-time discretizations of the TDVP equations of motion break the symplectic structure, though it remains to be understood at which order in the time step this occurs. As an independent test of the magnitude of numerical errors, we use the product of the magnitudes of Jacobian eigenvalues. Due to the preservation of the phase space volume, this is expected to be equal to 1. For periodic orbits, we have typically obtained a product of eigenvalues that differs from 1 by less than 0.1 for unstable orbits and less than 0.01 for stable orbits.

# 3. Onset of instability for a $\chi = 2$ periodic orbit

In Sec. III C, we have observed that by changing the coupling J, the nature of the periodic orbit changes from stable to unstable. Here, we study this transition in more detail. In particular, we look at the evolution of all Floquet multipliers (eigenvalues of the Jacobian) in the complex plane (see Fig. 7). Before instability, for J = 1.25, we observe that all  $2\chi^2 = 8$  eigenvalues live on the unit circle in the complex plane, with four of them located near -1, and the remaining four distributed over the circle (not visible due to overlap with other dots corresponding to higher J). Upon increasing J, we note that a pair among the four eigenvalues near -1 approach -1. This pair "collides" at the point of the instability, and past the onset of instability at J = 1.275 one of the eigenvalues becomes larger than 1 and moves outside of the unit circle, whereas the second eigenvalue moves inside. Even further away, at J = 1.3 we note that there are already four eigenvalues not on the unit circle.

Observing that a pair of multipliers that were previously on the unit circle are now on the real line and on opposite sides of -1, we assume that -1 has been crossed with increasing J, which points at a (supercritical) period-doubling (also known as "flip") bifurcation [93] at some J

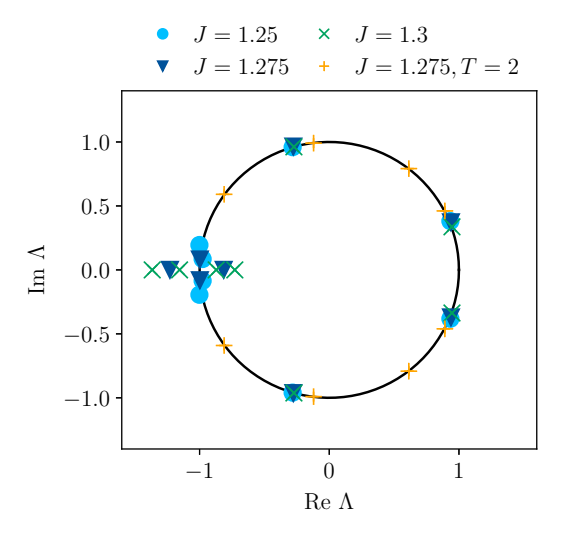


FIG. 7. The evolution of Floquet multipliers of the GS orbit in the complex plane upon changing the coupling J in the kicked Ising model. For a stable orbit, all Floquet multipliers lie on the unit circle. Upon increasing J, we observe that two (J = 1.275) and then four (J = 1.3) Floquet multipliers collide and then move away from the unit circle. This indicates the onset of instability. The orange triangles correspond to the period-doubled stable orbit that we find for the value of coupling past the instability onset.

between J=1.25 and J=1.275. However, we have been unable to find the stable double-period orbit that would correspond to this bifurcation. While for J=1.275 we have found a stable double-period orbit (its stability is recorded in Fig. 7 with orange "+" marks), it does not branch from the stable period-1 orbit at J=1.25.

## 4. Nine-dimensional KAM torus for $\chi = 3$

In Sec. III B, for the J=1.09, we have discussed the properties of the stable orbit with  $\chi=2$ . In particular, using the dynamics of local observables when the system is initialized slightly away from the periodic orbit, we have visualized the four-dimensional KAM torus. The existence of the torus is already apparent from the fact that local observables remain very close to their values at the periodic orbit for long times. Understanding the dimensionality of the torus is more subtle, and we have confirmed it by matching the peaks in the Fourier spectrum to the phases of Jacobian eigenvalues. The four-dimensional nature of the torus, identified by the four different frequencies, is consistent with the expectations of having a  $\chi^2$  dimensional torus for a generic stable periodic orbit in an MPS manifold with bond dimension  $\chi$ .

In order to further confirm these expectations, we have studied the properties of the periodic orbit with  $\chi = 3$  found at the value of coupling J = 0.91. Perturbing the orbit by  $\Delta = 10^{-5}$ , we compute the stroboscopic expectation values of observables for times nT with  $n \in [1,500]$ .

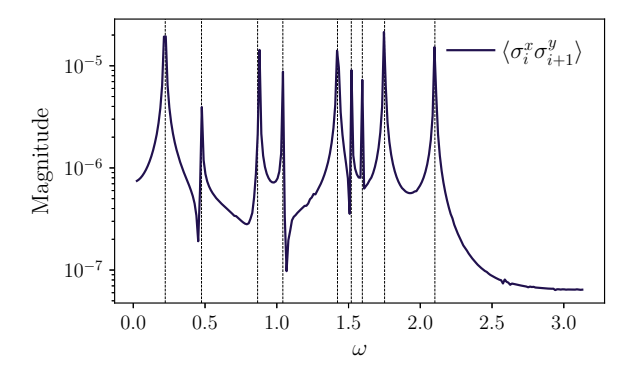


FIG. 8. The  $\chi=3$  stable periodic orbit for J=0.91. The frequencies from the Jacobian are the same as those from the Fourier transform of the signal. The excess entanglement accumulated in the exact dynamics compared to the entanglement on the orbit is  $\delta S_{\rm ent}=0.11$ . Comparing this value with Fig. 3, we conclude that this is an intermediate-leakage orbit.

The corresponding Fourier spectra are also compared with the phases obtained from the Floquet multipliers. We note that the analysis of single-spin expectation values  $\langle \sigma^{\alpha} \rangle$  with  $\alpha = x, y, z$  has revealed only eight, instead of the expected nine, peaks. However, analyzing more complicated two-site observables such as  $\langle \sigma_i^x \sigma_{i+1}^y \rangle$  shown in Fig. 8 yields the expected  $\chi^2 = 9$  peaks that also match the phases of the eigenvalues of the Jacobian. Therefore, we further support our conclusion about the generic occurrence of  $\chi^2$ -dimensional KAM tori around stable periodic orbits. In addition, we note that with increasing bond dimension, progressively more dynamical variables are involved in describing the correlations of the system, hence suggesting that stability analysis requires input beyond single-spin expectation values.

# 5. Comparison of orbits with different bond dimensions

In the main text, we have illustrated the existence of multiple periodic orbits for different values of the bond dimension  $\chi = 1, \dots, 4$ . This leads to the natural question of whether the orbits found at different values of  $\chi$  are related among themselves and potentially also to the eigenstates of the unitary in Eq. (16). To investigate this potential relation, we study the pairwise distances between orbits at t = 0 using fidelity in Eq. (11).

In Fig. 9, we show the fidelity between the initial points of different orbits. The first periodic orbit  $\chi=1$  is a ceiling state from the main text, and according to the figure, it has relatively small overlaps (at most 0.7) with all remaining orbits. On the other hand, the second orbit found for  $\chi=1$  has a partner  $\chi=2$  orbit, as is witnessed by the considerably larger overlap of 0.95. This partner orbit has been analyzed in Sec. III C, where it has been shown to be a ground state of the effective Hamiltonian. Note that we

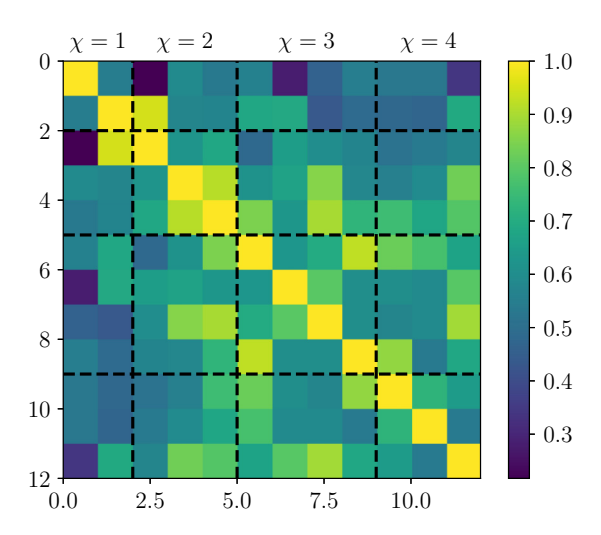


FIG. 9. The fidelity between initial points of orbits for different values of  $\chi$ .

have not found further relatives of this orbit at higher bond dimensions (note the absence of bright colors in the  $\chi > 2$  parts of the second row or column of the matrix in Fig. 9). The relation between orbits can also be seen in Fig. 11 in Appendix C 2 below, where we illustrate the overlap of the initial points of the orbit with eigenstates of the effective Hamiltonian.

In contrast to the first  $\chi = 2$  orbit, the second and third  $\chi = 2$  orbits have partners in  $\chi = 3$  and  $\chi = 4$ , as is evidenced by the overlap of 0.86 and 0.83 for the second orbit and 0.9 and 0.8 for the third one. Despite the intuition that orbits with higher bond dimensions should better represent the eigenstates of the effective Hamiltonian, in Fig. 4, we do not see a qualitative difference in the IPR scaling between orbits with different  $\chi$ . One reason for this may be the higher leakage of the underlying orbits, as the correspondence between eigenstates and orbits is expected to hold only in the low-leakage regime. Another reason may be related to the algorithm for finding the periodic orbits. As we have discussed above in Appendices A 1 and A 3, the canonical form and gradient-descent algorithms may experience numerical-stability issues when converging to the state with an effective lower bond dimension.

# APPENDIX C: QUANTUM PROPERTIES OF THE PERIODIC ORBITS

In this appendix, we provide additional details on the prethermal regime of the kicked Ising model and calculate the overlaps of states corresponding to periodic orbits with eigenstates of the effective Hamiltonian.

### 1. Prethermal regime

In this section, we discuss the prethermal regime of the kicked Ising model in Eq. (16). To test at which values of

coupling J the system thermalizes, we check if its eigenstates obey the Floquet eigenstate thermalization hypothesis (ETH) [9,45–48]. For this, we compute the propagator in Eq. (16) for L=14 with momentum block k=0 and parity block +1 for periodic boundary conditions using the QuSpin software package [94,95] and perform exact diagonalization to find eigenstates  $|\varphi_n\rangle$ ,

$$U_T|\varphi_n\rangle = E_n|\varphi_n\rangle,$$
 (C1)

and corresponding eigenvalues  $E_n$ . The Floquet Hamiltonian relates to the propagator as  $H_F = i \ln U_T$ , and so the spectrum of the Floquet Hamiltonian is related to that of the propagator

$$e_n = i \ln E_n. \tag{C2}$$

In the thermal regime, we expect that expectation values of local observables vary only slightly between eigenstates with nearby energies and fluctuate around zero—their infinite-temperature expectation value. In contrast, in the prethermal phase, the eigenstates can be obtained from folding the spectrum of the approximate local effective Hamiltonian. Hence, we expect to see the deviations from the typical thermal values.

In Fig. 10, we show a local-observable expectation value versus the quasienergy values for two different values of J. The behavior at the dual-unitary point,  $J = \pi/2$ , where magnetization fluctuates around zero, should be contrasted to the behavior at the smaller value of J = 1.09, where traces of smooth, systematic dependence on the quasienergy are visible, suggesting that the system is still in the prethermal regime. The transition from the prethermal regime to the thermal regime leads to the eigenstates of the effective Hamiltonian becoming more and more thermal. This leads to the higher leakage of periodic orbits, which we observe in Fig. 3(c) (top panel) when increasing coupling J.

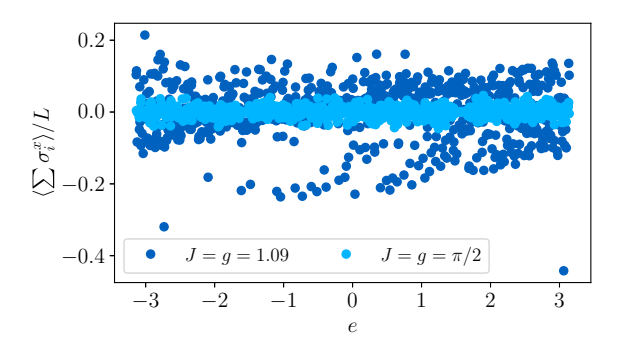


FIG. 10. The magnetization along the x direction for different J in a spin chain of size L=14, momentum block 0, and parity block +1. For the smaller value of J, the systematic dependence on e highlights a prethermal regime, whereas at the dual-unitary point, the magnetization fluctuates around zero.

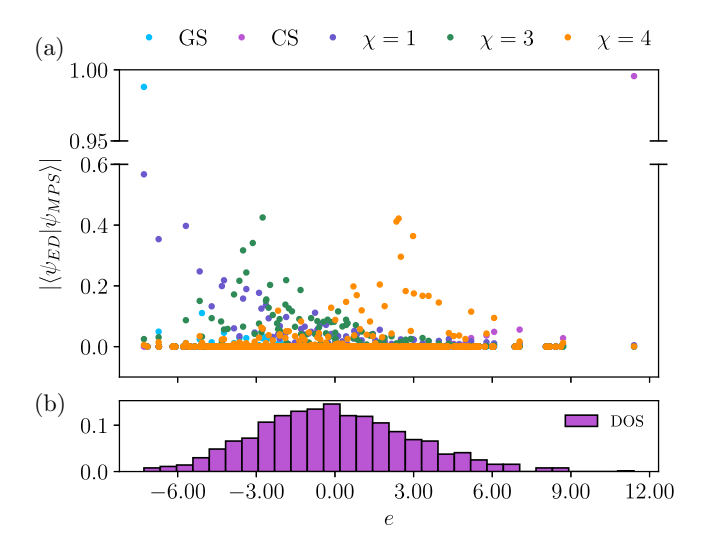


FIG. 11. (a) The overlap of some MPSs corresponding to the periodic orbits and eigenstates of the fourth-order effective Hamiltonian for J=1.09 and L=10. (b) The normalized density of states (DOS) of the  $H_{\rm eff}^4$ . The different colors of dots correspond to the periodic orbits from Fig. 1. The states corresponding to the least leaky periodic orbits have an overlap of order 1 with the ground and ceiling states of the effective Hamiltonian. One  $\chi=1$  orbit also has a high overlap with the GS, while the  $\chi=3,4$  orbits have the highest overlap with the states from the middle of the spectra.

#### 2. Effective Hamiltonian

To understand the role of periodic orbits in the prethermal regime, we study the overlap of the MPS corresponding to the periodic orbit with the eigenstates of the effective Hamiltonian  $H_{\rm eff}^{(4)}$ , which is obtained from the fourth-order Magnus expansion of Eq. (16). In the kicked model, the Magnus expansion simplifies to the Baker-Campbell-Hausdorff formula,

$$U_{T} = \exp\left(-i\frac{1}{2}H_{2}\right) \exp\left(-i\frac{1}{2}H_{1}\right) \approx \exp(-iTH_{\text{eff}}^{(4)}),$$

$$H_{\text{eff}}^{(4)} = \frac{1}{2}(H_{1} + H_{2}) - \frac{i}{8}[H_{2}, H_{1}] + \frac{1}{96}([H_{1}, [H_{1}, H_{2}]]) + [H_{2}, [H_{2}, H_{1}]]) - \frac{i}{384}([H_{2}, [H_{1}, [H_{1}, H_{2}]]]),$$
(C3)

leading to a translationally invariant Hamiltonian with terms including products of up to five Pauli matrices.

We construct the effective Hamiltonian  $H_{\text{eff}}^{(4)}$  using the QuSpin [94,95] software package for L=10 in the full Hilbert space and diagonalize it to obtain all energies  $(e_n)$  and eigenvectors. In Fig. 11, we show the overlap of the eigenvectors of the effective Hamiltonian in Eq. (C3) with the MPSs corresponding to some of the periodic orbits from Fig. 1. The two low-leakage periodic orbits (GS and CS in Fig. 1) correspond to the ground and ceiling

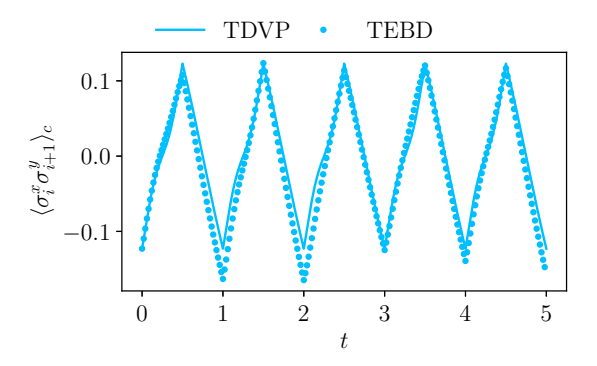


FIG. 12. The connected correlation-function dynamics of the GS trajectory obtained by TDVP (full line) and TEBD (dotted line) simulations.

states of the effective Hamiltonian, as is witnessed by their overlaps being close to 1 in Fig. 11. We also illustrate another  $\chi=1$  orbit, as it has a high overlap with the ground state. In Fig. 12, we illustrate the comparison of the correlation function during the TDVP and exact dynamics represented by TEBD. The figure illustrates that the dynamics of low-leakage trajectories are very close to the exact dynamics.

In contrast, the other MPSs corresponding to more leaky periodic orbits have the largest overlaps with eigenstates of the effective Hamiltonian from the middle of the spectrum (For clarity, only two such orbits labeled as  $\chi = 3,4$ are shown in Fig. 11). These overlaps have a maximum at a certain energy and decay exponentially with energy difference (not shown). This is in contrast to the DMRG approximation of ground states of local Hamiltonians, where overlap has been found to have flat tails [96], and resembles the energy distribution of states obtained from imaginary time evolution. Since these MPSs have a low bond dimension,  $\chi \leq 4$ , the fact that they have overlaps on the order of 0.5 with individual eigenstates is still highly unusual. This suggests that even the effective Hamiltonian in Eq. (C3) may not be fully thermal, at least for the considered system size. We defer the systematic investigation of the ETH for the effective Hamiltonian and potential relation of periodic orbits to quantum many-body scars [73–82] to future work.

# APPENDIX D: ORBIT SEARCH IN HAMILTONIAN MODELS

In this appendix, we demonstrate the extension of our method to Hamiltonian models. First, we briefly discuss a gradient-based search for the orbit period. We then present the results of the orbit search in the deformed XXZ and XYZ models.

## 1. Modification of the algorithm

For Hamiltonian models, searching for periodic orbits requires an additional optimization step over the period T. We implement the same algorithm as described in the main text, extended to include the gradient with respect to the period. The loss function now depends on both  $A_L$  and the period T. The derivative with respect to the period is computed as

$$\delta t = \frac{F(A_L, T - \Delta t) - F(A_L, T + \Delta t)}{2\Delta t}.$$
 (D1)

We run many randomly initialized states, with the initial guess for the period initialized randomly in the interval [1, 3].

We emphasize that, in contrast to the Floquet setting, the dynamics generated by a fixed Hamiltonian conserve energy. This energy conservation also holds for the TDVP projection. However, implementing energy conservation within the gradient-descent updates to the MPS in the trajectory search is nontrivial. The present implementation of the orbits search does not conserve the energy, allowing the gradient-based update to move between different energy shells. This leads to the algorithm finding a subset of all possible periodic orbits that nevertheless show interesting physics. We reserve the implementation of orbit search restricted to a fixed energy shell for future work.

## 2. XXZ model

We consider the XXZ spin-1/2 model with magnetic fields applied along the x and z directions. The field in the x direction acts as an integrability-breaking deformation that also removes the conservation of total z magnetization. The resulting Hamiltonian reads

$$H = \frac{1}{4} \sum_{i} \left[ J(\sigma_i^x \sigma_{i+1}^x + \sigma_i^y \sigma_{i+1}^y) + \Delta \sigma_i^z \sigma_{i+1}^z + 2h_x \sigma_i^x + 2h_z \sigma_i^z \right], \tag{D2}$$

where  $\sigma_i^{x,y,z}$  are the Pauli operators acting on site *i*. Running our algorithm for the parameters  $J=1, \Delta=-0.5, h_x=0.9$ , and  $h_z=2$ , and bond dimensions  $\chi=2,3,4$ , we find periodic orbits with precisions  $10^{-6}, 10^{-7}$ , and  $10^{-8}$ , respectively. In Fig. 13, we illustrate the dynamics of the local observables, correlation functions, and entanglement along these orbits.

We note that many orbit searches converge to stationary states (zero-period orbits) or local minima. The increased tendency of convergence to the zero-period orbits compared to the Floquet case can be attributed to the absence of energy conservation. Moving across energy shells enables the algorithm to find approximate eigenstates of the Hamiltonian at the edges of the spectrum, that correspond to stationary points of the flow. Indeed, the eigenstates at

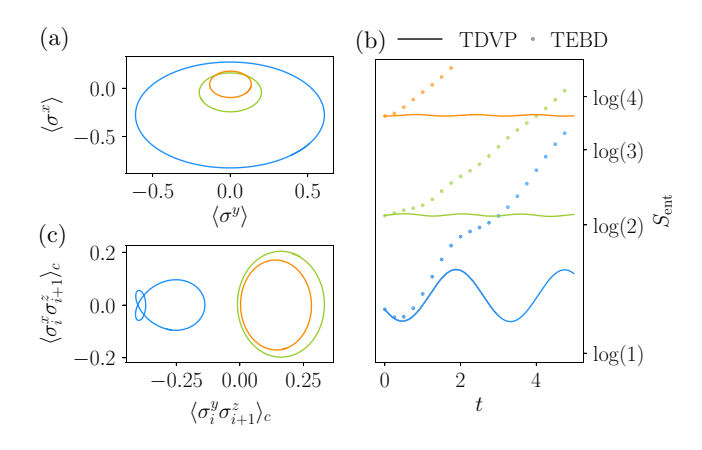


FIG. 13. Periodic orbits for different bond dimensions for the deformed XXZ Hamiltonian in Eq. (D2). The periods for the trajectories are T=2.86, 1.55, 1.57 for  $\chi=2,3,4$  correspondingly. (a) The dynamics of local observables over the period. (b) The entanglement-entropy dynamics of the TDVP trajectory and the exact quantum dynamics (TEBD, N=50). All three trajectories show big differences in the entanglement entropy, suggesting that all trajectories have significant leakage. (c) The dynamics of the two-point-connected correlation functions.

the edges of the energy spectrum can feature low entanglement, and thus may be effectively approximated by a low-bond-dimension MPS. In this sense, our algorithm for Hamiltonian systems is capable of reproducing DMRG results [61,62]. Nevertheless, in addition to stationary approximations to eigenstates, our method also converges to periodic orbits with nonzero period. These solutions possess a full Schmidt rank, indicating that they are entangled, and they lie far from simple product states in the Hilbert space.

In Fig. 13(b), we suggest that the discovered orbits feature significant leakage; thus we expect to see agreement between the exact unitary and TDVP dynamics only at short times. At the same time, the study of the many-body eigenstates of the Hamiltonian in Eq. (D2) reveals characteristic towers in the overlap  $|\langle \psi_{\text{MPS}} | \psi_{E_n} \rangle|^2$ , where  $\{\psi_{E_n}\}$  are the exact eigenstates, and  $\psi_{\text{MPS}}$  is the initial point on the MPS orbit with  $\chi = 4$  (see Fig. 14).

Similar towers have been observed for quantum many-body scars in the PXP model [73] for the overlaps with the Néel initial product state. In contrast, for our system, the overlaps show towerlike structure for the short-range entangled MPS state with  $\chi=4$  obtained from the orbit-search algorithm. The energy distance between towers approximately corresponds to  $2\pi/T$ , where T=1.57 is the oscillation period of the MPS orbit, and towers are peaking close to the middle of the spectrum, illustrating that we uncover high-energy-density scars. At the same time, the plot in Fig. 14(b) reveals that almost all eigenstates of the deformed XXZ model feature small fluctuations in the

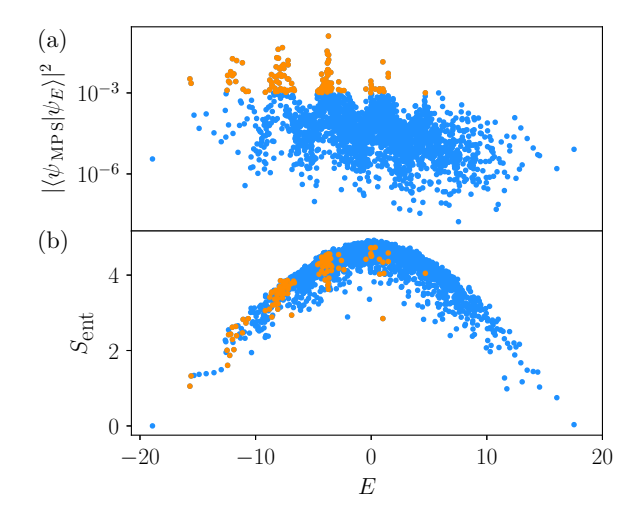


FIG. 14. (a) The overlap of the MPS state for the  $\chi=4$  orbit with the spectra of the Hamiltonian in the zero-momentum and even-parity sector, for system size L=16. Towers around specific states indicate that the MPS state mostly expands over sets of eigenstates, which are close to equidistant in their eigenvalues. (b) This plot shows that eigenstates with anomalously large overlap with the MPS state (shown in orange) feature large bipartite entanglement.

bipartite-entanglement entropy, with only a few outliers. Therefore, finding these eigenstates without the MPS orbit search would not be possible.

For the chosen parameters, the XXZ model with transverse and longitudinal fields is nonintegrable, and the level-spacing statistics of its spectrum follow a Wigner-Dyson distribution, characteristic of quantum chaotic systems. This suggests that the periodic trajectories that we find are embedded within a chaotic spectral background, yet remain structured enough to have strong overlap with a specific subset of eigenstates. While a detailed understanding of the emergence of scars in the deformed XXZ model is beyond the scope of our work, we track the fate of the MPS orbit with changing single-particle fields.

We follow the fate of the orbit found  $h_z = 2$  by changing the value of  $h_z$  by small increments between 0.1 and 0.2, and initializing the algorithm at the MPS tensors corresponding to the orbit at the previous value of  $h_z$ . We plot the difference in entanglement entropy for TEBD and TDVP evolutions at time T = 10 across the investigated values of  $h_z$  in Fig. 15. Upon decreasing  $h_z$ , the leakage grows, peaking around  $h_z = 1.6$ , and the algorithm fails to find the orbit for somewhat smaller values of the field. In this sense, our orbit seems not to be related to stable periodic orbits constructed in Ref. [97]. In contrast, increasing the value of  $h_z$  leads to a decrease in the leakage, suggesting that potentially the fate of the orbit and emergence of scars in the deformed XXZ model may be understood starting from the large- $h_z$  limit.

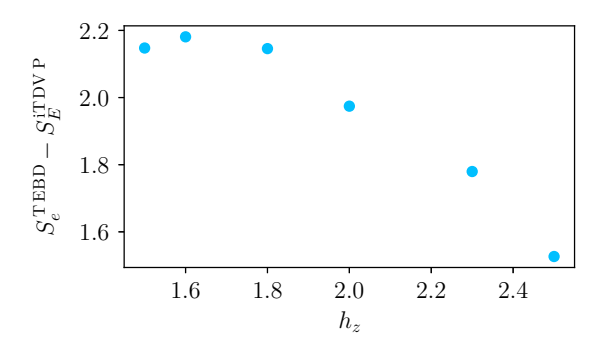


FIG. 15. The difference of entanglement entropy for the TEBD and TDVP dynamics at T = 10 for the  $\chi = 4$  periodic trajectories for different field  $h_z$ . Increasing the field  $h_z$ , the MPS orbit is getting less entangled, and the difference in the entanglement between projected and exact time evolution that characterizes leakage decreases.

### 3. XYZ model

The XYZ spin chain, characterized by anisotropic couplings along the three spin directions, represents one of the most general integrable nearest-neighbor spin- $\frac{1}{2}$  models [98]:

$$H = \frac{1}{4} \sum_{i} \left[ J_{x} \sigma_{i}^{x} \sigma_{i+1}^{x} + J_{y} \sigma_{i}^{y} \sigma_{i+1}^{y} + J_{z} \sigma_{i}^{z} \sigma_{i+1}^{z} \right], \quad (D3)$$

where  $J_x$ ,  $J_y$ , and  $J_z$  denote the interaction strengths in the x, y, and z directions, respectively. By tuning these parameters, one can interpolate between different limiting cases such as the XXZ and XY models, while in the fully anisotropic regime ( $J_x \neq J_y \neq J_z$ ), the system features no additional symmetries beyond spatial inversion and translation

In our study, we focus on the parameter set  $J_x = 0.6$ ,  $J_y = 1$ , and  $J_z = 0.5$ . In this case, we identify two nontrivial periodic trajectories with bond dimension  $\chi = 4$  converged to numerical precision of order  $10^{-7}$ . The dynamics of their entanglement spectra (Schmidt coefficients) are shown in Fig. 16. In Fig. 16(b), we illustrate that these trajectories feature nontrivial dynamics of correlation

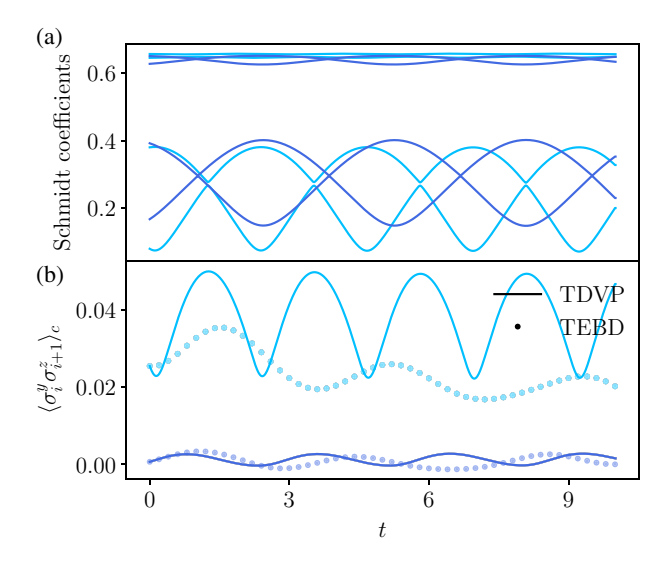


FIG. 16. (a) The Schmidt coefficient dynamics for two trajectories with  $\chi=4$  for the XYZ Hamiltonian. The period of the light-blue trajectory is T=2.28, while for the deep blue, the period is T=2.82. (b) The TDVP dynamics of the two-point correlation function. The exact unitary dynamics obtained with TEBD also show oscillations but do not agree well with the TDVP, especially for the light-blue trajectory, due to the large leakage.

functions, yet are characterized by relatively large leakage. In contrast, all other optimization runs converged to local minima or produced trajectories that appeared stationary under the TDVP dynamics. The increased convergence of the orbit-search algorithm to stationary points hints that periodic orbits feature qualitatively different structures between flows generated by chaotic and integrable models. Also, individual scarred eigenstates have recently been reported in XYZ models [99], although they typically feature translational invariance with a larger unit cell. The detailed investigation of this phenomenon is beyond the scope of the present work.

The trajectories found by our algorithm exhibit a large overlap with weakly entangled states that lie closer to the boundary of the finite-size Hamiltonian spectrum [see

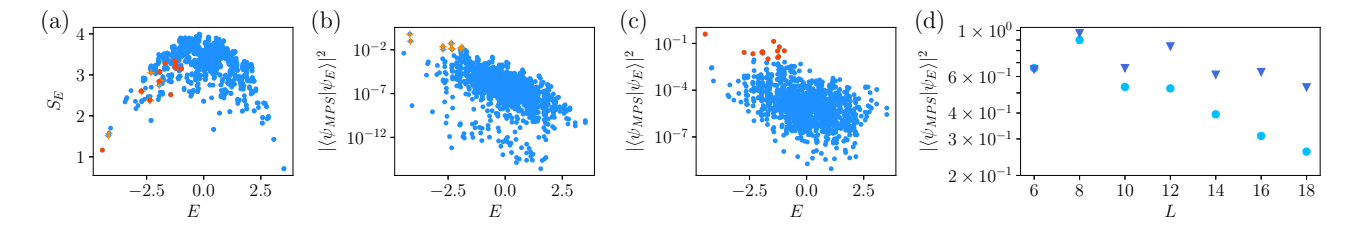


FIG. 17. (a) The bipartite entanglement of all eigenstates of the XYZ model for L=12 in the zero-momentum sector. (b),(c) Overlaps of all eigenstates for two found trajectories with the MPS state on the orbits for the same system size show outliers, but this time located at lower energy densities. (d) The finite-size scaling of the overlaps with the ground state and first excited state for found trajectories. One trajectory (light blue) always has the highest overlap with the GS, while the second one (dark blue) has the highest overlap with GS for L=4k+2 and with the first excited state for L=4k. In the figure, we show the scaling of the highest overlap.

Figs. 17(a)–17(c)]. Although the overlap is nominally largest between the MPS and ground state or the first excited state, the single (approximate) eigenstate is incapable of producing nontrivial dynamics of local observables and correlation functions reported in Fig. 16. Hence, the excitations above the ground state are expected to play a nontrivial role, and indeed, we see in Fig. 17(d) that the largest overlap between MPS and a particular eigenstate (ground state or first excited state) is decreasing exponentially with the system size. This suggests that our MPS trajectory will correspond to a nontrivial combination of eigenstates at the finite energy density in the thermodynamic limit, potentially leading to the identification of trajectory-related finite-energy-density scars in the XYZ model.

- [1] F. Haake, *Quantum Signatures of Chaos* (Springer, Berlin, 1991).
- [2] O. Bohigas, M.-J. Giannoni, and C. Schmit, Characterization of chaotic quantum spectra and universality of level fluctuation laws, Phys. Rev. Lett. 52, 1 (1984).
- [3] M. V. Berry, and M. Tabor, Level clustering in the regular spectrum, Proc. R. Soc. London. A. Math. Phys. Sci. 356, 375 (1977).
- [4] A. I. Larkin, and Y. N. Ovchinnikov, Quasiclassical method in the theory of superconductivity, Sov. Phys. JETP 28, 1200 (1969).
- [5] B. Swingle, G. Bentsen, M. Schleier-Smith, and P. Hayden, Measuring the scrambling of quantum information, Phys. Rev. A 94, 040302(R) (2016).
- [6] Y. Huang, Y.-L. Zhang, and X. Chen, Out-of-time-ordered correlators in many-body localized systems, Ann. Phys. 529, 1600318 (2017).
- [7] E. B. Rozenbaum, S. Ganeshan, and V. Galitski, Lyapunov exponent and out-of-time-ordered correlator's growth rate in a chaotic system, Phys. Rev. Lett. 118, 086801 (2017).
- [8] V. Oganesyan, and D. A. Huse, Localization of interacting fermions at high temperature, Phys. Rev. B—Condens. Matter Mater. Phys. 75, 155111 (2007).
- [9] L. D'Alessio, Y. Kafri, A. Polkovnikov, and M. Rigol, From quantum chaos and eigenstate thermalization to statistical mechanics and thermodynamics, Adv. Phys. 65, 239 (2016).
- [10] L. F. Santos, and M. Rigol, Onset of quantum chaos in onedimensional bosonic and fermionic systems and its relation to thermalization, Phys. Rev. E—Stat. Nonlin. Soft Matter Phys. 81, 036206 (2010).
- [11] A. M. Kaufman, M. E. Tai, A. Lukin, M. Rispoli, R. Schittko, P. M. Preiss, and M. Greiner, Quantum thermalization through entanglement in an isolated many-body system, Science 353, 794 (2016).
- [12] C. Neill, P. Roushan, M. Fang, Y. Chen, M. Kolodrubetz, Z. Chen, A. Megrant, R. Barends, B. Campbell, B. Chiaro et al., Ergodic dynamics and thermalization in an isolated quantum system, Nat. Phys. 12, 1037 (2016).
- [13] S. Scherg, T. Kohlert, P. Sala, F. Pollmann, B. Hebbe Madhusudhana, I. Bloch, and M. Aidelsburger, Observing

- non-ergodicity due to kinetic constraints in tilted Fermi-Hubbard chains, Nat. Commun. **12**, 4490 (2021).
- [14] D. Bluvstein, A. Omran, H. Levine, A. Keesling, G. Semeghini, S. Ebadi, T. T. Wang, A. A. Michailidis, N. Maskara, W. W. Ho *et al.*, Controlling quantum many-body dynamics in driven Rydberg atom arrays, Science 371, 1355 (2021).
- [15] W. Morong, F. Liu, P. Becker, K. Collins, L. Feng, A. Kyprianidis, G. Pagano, T. You, A. Gorshkov, and C. Monroe, Observation of Stark many-body localization without disorder, Nature 599, 393 (2021).
- [16] A. Lerose, M. Sonner, and D. A. Abanin, Scaling of temporal entanglement in proximity to integrability, Phys. Rev. B 104, 035137 (2021).
- [17] M. Bukov, S. Gopalakrishnan, M. Knap, and E. Demler, Prethermal Floquet steady states and instabilities in the periodically driven, weakly interacting Bose-Hubbard model, Phys. Rev. Lett. 115, 205301 (2015).
- [18] P. M. Schindler, and M. Bukov, Geometric Floquet theory, Phys. Rev. X 15, 031037 (2025).
- [19] A. A. Michailidis, C. J. Turner, Z. Papić, D. A. Abanin, and M. Serbyn, Slow quantum thermalization and many-body revivals from mixed phase space, Phys. Rev. X 10, 011055 (2020).
- [20] P. Doria, T. Calarco, and S. Montangero, Optimal control technique for many-body quantum dynamics, Phys. Rev. Lett. 106, 190501 (2011).
- [21] G. Cecile, H. Lóio, and J. De Nardis, Measurement-induced phase transitions by matrix product states scaling, Phys. Rev. Res. 6, 033220 (2024).
- [22] G. Vidal, Efficient classical simulation of slightly entangled quantum computations, Phys. Rev. Lett. **91**, 147902 (2003).
- [23] G. Vidal, Efficient simulation of one-dimensional quantum many-body systems, Phys. Rev. Lett. **93**, 040502 (2004).
- [24] G. Vidal, Classical simulation of infinite-size quantum lattice systems in one spatial dimension, Phys. Rev. Lett. 98, 070201 (2007).
- [25] P. A. Dirac, in *Mathematical Proceedings of the Cambridge Philosophical Society*, (Cambridge University Press, Cambridge, 1930), Vol. 26, p. 376.
- [26] C. Lubich, From Quantum to Classical Molecular Dynamics: Reduced Models and Numerical Analysis (European Mathematical Society, Zürich, Zurich, 2008), Vol. 12.
- [27] J. Frenkel, *Wave Mechanics: Advanced General Theory* (Clarendon Press, Oxford, United Kingdom, 1934).
- [28] J. Haegeman, J. I. Cirac, T. J. Osborne, I. Pižorn, H. Verschelde, and F. Verstraete, Time-dependent variational principle for quantum lattices, Phys. Rev. Lett. 107, 070601 (2011).
- [29] A. Hallam, J. Morley, and A. G. Green, The Lyapunov spectra of quantum thermalisation, Nat. Commun. 10, 2708 (2019).
- [30] W. W. Ho, S. Choi, H. Pichler, and M. D. Lukin, Periodic orbits, entanglement, and quantum many-body scars in constrained models: Matrix product state approach, Phys. Rev. Lett. **122**, 040603 (2019).
- [31] P. Cvitanović, R. Artuso, R. Mainieri, G. Tanner, and G. Vattay, *Chaos: Classical and Quantum* (Niels Bohr Institute, Copenhagen, 2020).

- [32] R. Artuso, E. Aurell, and P. Cvitanović, Recycling of strange sets: I. Cycle expansions, Nonlinearity 3, 325 (1990).
- [33] R. Artuso, E. Aurell, and P. Cvitanović, Recycling of strange sets: II. Applications, Nonlinearity 3, 361 (1990).
- [34] P. Cvitanović, Periodic orbits as the skeleton of classical and quantum chaos, Physica D 51, 138 (1991).
- [35] J.-P. Eckmann, and D. Ruelle, Ergodic theory of chaos and strange attractors, Rev. Mod. Phys. 57, 617 (1985).
- [36] J. Guckenheimer, and B. Meloon, Computing periodic orbits and their bifurcations with automatic differentiation, SIAM J. Sci. Comput. 22, 951 (2000).
- [37] U. M. Ascher, R. M. Mattheij, and R. D. Russell, Numerical Solution of Boundary Value Problems for Ordinary Differential Equations (SIAM, Philadelphia, 1995).
- [38] E. Hairer, G. Wanner, and S. P. Nørsett, Solving Ordinary Differential Equations I: Nonstiff Problems (Springer, Berlin, 1993).
- [39] M. Akila, D. Waltner, B. Gutkin, and T. Guhr, Particle-time duality in the kicked Ising spin chain, J. Phys. A: Math. Theor. 49, 375101 (2016).
- [40] B. Bertini, P. Kos, and T. Prosen, Exact spectral form factor in a minimal model of many-body quantum chaos, Phys. Rev. Lett. 121, 264101 (2018).
- [41] B. Bertini, P. Kos, and T. Prosen, Exact correlation functions for dual-unitary lattice models in 1 + 1 dimensions, Phys. Rev. Lett. 123, 210601 (2019).
- [42] B. Bertini, P. Kos, and T. Prosen, Entanglement spreading in a minimal model of maximal many-body quantum chaos, Phys. Rev. X 9, 021033 (2019).
- [43] L. Piroli, B. Bertini, J. I. Cirac, and T. Prosen, Exact dynamics in dual-unitary quantum circuits, Phys. Rev. B 101, 094304 (2020).
- [44] A. Lerose, M. Sonner, and D. A. Abanin, Influence matrix approach to many-body Floquet dynamics, Phys. Rev. X 11, 021040 (2021).
- [45] L. D'Alessio, and A. Polkovnikov, Many-body energy localization transition in periodically driven systems, Ann. Phys. 333, 19 (2013).
- [46] A. Lazarides, A. Das, and R. Moessner, Equilibrium states of generic quantum systems subject to periodic driving, Phys. Rev. E **90**, 012110 (2014).
- [47] T. Mori, T. Kuwahara, and K. Saito, Rigorous bound on energy absorption and generic relaxation in periodically driven quantum systems, Phys. Rev. Lett. 116, 120401 (2016).
- [48] T. Mori, T. N. Ikeda, E. Kaminishi, and M. Ueda, Thermalization and prethermalization in isolated quantum systems: A theoretical overview, J. Phys. B: At., Mol. Opt. Phys. 51, 112001 (2018).
- [49] B. Neyenhuis, J. Zhang, P. W. Hess, J. Smith, A. C. Lee, P. Richerme, Z.-X. Gong, A. V. Gorshkov, and C. Monroe, Observation of prethermalization in long-range interacting spin chains, Sci. Adv. 3, e1700672 (2017).
- [50] W. W. Ho, T. Mori, D. A. Abanin, and E. G. Dalla Torre, Quantum and classical Floquet prethermalization, Ann. Phys. 454, 169297 (2023).
- [51] T. N. Ikeda, S. Sugiura, and A. Polkovnikov, Robust effective ground state in a nonintegrable Floquet quantum circuit, Phys. Rev. Lett. **133**, 030401 (2024).

- [52] A. N. Kolmogorov, in *Dokl. akad. nauk Sssr* (USSR Academy of Sciences, Moscow, 1954), Vol. 98, p. 527.
- [53] J. Möser, On invariant curves of area-preserving mappings of an annulus, Nachr. Akad. Wiss. Göttingen, II, 1 (1962).
- [54] V. I. Arnold, Proof of a theorem of A. N. Kolmogorov on the invariance of quasi-periodic motions under small perturbations of the Hamiltonian, in *Collected Works: Rep*resentations of Functions, Celestial Mechanics and KAM Theory, 1957–1965 (Springer, Berlin, 2009), p. 267.
- [55] E. Ott, *Chaos in Dynamical Systems* (Cambridge University Press, Cambridge, 2002).
- [56] C. Fleckenstein, and M. Bukov, Thermalization and prethermalization in periodically kicked quantum spin chains, Phys. Rev. B 103, 144307 (2021).
- [57] L. Vanderstraeten, J. Haegeman, and F. Verstraete, Tangent-space methods for uniform matrix product states, SciPost Physics Lecture Notes, 007 (2019).
- [58] V. Zauner-Stauber, L. Vanderstraeten, M. T. Fishman, F. Verstraete, and J. Haegeman, Variational optimization algorithms for uniform matrix product states, Phys. Rev. B 97, 045145 (2018).
- [59] Y. Wu, Time-dependent variational principle for mixed matrix product states in the thermodynamic limit, Phys. Rev. B 102, 134306 (2020).
- [60] H. Kim, and D. A. Huse, Ballistic spreading of entanglement in a diffusive nonintegrable system, Phys. Rev. Lett. 111, 127205 (2013).
- [61] D. Perez-Garcia, F. Verstraete, M. M. Wolf, and J. I. Cirac, Matrix product state representations, Quantum Inf. Comput. 7, 401 (2007).
- [62] J. I. Cirac, D. Pérez-García, N. Schuch, and F. Verstraete, Matrix product states and projected entangled pair states: Concepts, symmetries, theorems, Rev. Mod. Phys. 93, 045003 (2021).
- [63] We believe that our method can be extended to noninjective MPSs, which are relevant in scenarios involving spontaneous symmetry breaking. However, a detailed investigation of this case is left for future work.
- [64] V. Zauner, D. Draxler, L. Vanderstraeten, M. Degroote, J. Haegeman, M. M. Rams, V. Stojevic, N. Schuch, and F. Verstraete, Transfer matrices and excitations with matrix product states, New J. Phys. 17, 053002 (2015).
- [65] L. E. Fischer, M. Leahy, A. Eddins, N. Keenan, D. Ferracin, M. A. Rossi, Y. Kim, A. He, F. Pietracaprina, B. Sokolov et al., Dynamical simulations of many-body quantum chaos on a quantum computer, ArXiv:2411.00765.
- [66] For  $\chi = 1$  our algorithm essentially reduces to the dynamical mean-field theory, but for consistency we use the same code.
- [67] M. Fishman, S. R. White, and E. M. Stoudenmire, The ITensor Software Library for Tensor Network Calculations, SciPost Phys. Codebases, 4 (2022).
- [68] H. D. I. Abarbanel, R. Brown, and M. B. Kennel, Variation of Lyapunov exponents on a strange attractor, J. Nonlinear Sci. 1, 175 (1991).
- [69] E. Aurell, G. Boffetta, A. Crisanti, G. Paladin, and A. Vulpiani, Predictability in the large: An extension of the concept of Lyapunov exponent, J. Phys. A: Math. Gen. 30, 1 (1997).
- [70] S. R. White, Density matrix formulation for quantum renormalization groups, Phys. Rev. Lett. 69, 2863 (1992).

- [71] F. Verstraete, T. Nishino, U. Schollwöck, M. C. Bañuls, G. K. Chan, and M. E. Stoudenmire, Density matrix renormalization group, 30 years on, Nat. Rev. Phys. 5, 273 (2023).
- [72] N. Shiraishi, and T. Mori, Systematic construction of counterexamples to the eigenstate thermalization hypothesis, Phys. Rev. Lett. 119, 030601 (2017).
- [73] C. J. Turner, A. A. Michailidis, D. A. Abanin, M. Serbyn, and Z. Papić, Weak ergodicity breaking from quantum many-body scars, Nat. Phys. 14, 745 (2018).
- [74] M. Serbyn, D. A. Abanin, and Z. Papić, Quantum manybody scars and weak breaking of ergodicity, Nat. Phys. 17, 675 (2021).
- [75] S. Moudgalya, B. A. Bernevig, and N. Regnault, Quantum many-body scars and Hilbert space fragmentation: A review of exact results, Rep. Prog. Phys. **85**, 086501 (2022).
- [76] A. Chandran, T. Iadecola, V. Khemani, and R. Moessner, Quantum many-body scars: A quasiparticle perspective, Annu. Rev. Condens. Matter Phys. 14, 443 (2023).
- [77] M. Ljubotina, E. Petrova, N. Schuch, and M. Serbyn, Tangent space generators of matrix product states and exact Floquet quantum scars, PRX Quantum 5, 040311 (2024).
- [78] Q. Hummel, K. Richter, and P. Schlagheck, Genuine manybody quantum scars along unstable modes in Bose-Hubbard systems, Phys. Rev. Lett. 130, 250402 (2023).
- [79] B. Evrard, A. Pizzi, S. I. Mistakidis, and C. B. Dag, Quantum scars and regular eigenstates in a chaotic spinor condensate, Phys. Rev. Lett. 132, 020401 (2024).
- [80] I. Ermakov, O. Lychkovskiy, and B. V. Fine, Periodic classical trajectories and quantum scars in many-spin systems, ArXiv:2409.00258.
- [81] A. Pizzi, L.-H. Kwan, B. Evrard, C. B. Dag, and J. Knolle, Genuine quantum scars in many-body spin systems, Nat. Commun. 16, 6722 (2025).
- [82] B. Evrard, A. Pizzi, S. I. Mistakidis, and C. B. Dag, Quantum many-body scars from unstable periodic orbits, Phys. Rev. B 110, 144302 (2024).
- [83] V. I. Arnold, Doklady Akademii Nauk SSSR (USSR Academy of Sciences, Moscow, 1963), Vol. 152, p. 1249.
- [84] A. J. Lichtenberg, and M. A. Lieberman, Regular and Stochastic Motion (Springer, New York, 1983).

- [85] L. Zhang, V. Khemani, and D. A. Huse, A Floquet model for the many-body localization transition, Phys. Rev. B 94, 224202 (2016).
- [86] P. Ponte, Z. Papić, F. Huveneers, and D. A. Abanin, Manybody localization in periodically driven systems, Phys. Rev. Lett. 114, 140401 (2015).
- [87] A. Lazarides, A. Das, and R. Moessner, Fate of many-body localization under periodic driving, Phys. Rev. Lett. 115, 030402 (2015).
- [88] D. A. Abanin, W. De Roeck, and F. Huveneers, Theory of many-body localization in periodically driven systems, Ann. Phys. **372**, 1 (2016).
- [89] D. A. Abanin, E. Altman, I. Bloch, and M. Serbyn, Colloquium: Many-body localization, thermalization, and entanglement, Rev. Mod. Phys. **91**, 021001 (2019).
- [90] B. Sutherland, Beautiful Models: 70 Years of Exactly Solved Quantum Many-Body Problems (World Scientific Publishing Company, Singapore, 2004).
- [91] J. Ren, A. Hallam, L. Ying, and Z. Papić, ScarFinder: A detector of optimal scar trajectories in quantum many-body dynamics, PRX Quantum 6, 040332 (2025).
- [92] E. Petrova, 2025, https://github.com/alcien2/Finding-perio dic-orbits-with-iTDVP.git
- [93] Y. A. Kuznetsov, *Elements of Applied Bifurcation Theory* (Springer International Publishing, New York, 2023).
- [94] P. Weinberg, and M. Bukov, QUSPIN: A PYTHON package for dynamics and exact diagonalisation of quantum many body systems part I: Spin chains, SciPost Phys. 2, 003 (2017).
- [95] P. Weinberg, and M. Bukov, QUSPIN: A PYTHON package for dynamics and exact diagonalisation of quantum many body systems. part II: Bosons, fermions and higher spins, SciPost Phys. 7, 020 (2019).
- [96] J. M. Silvester, G. Carleo, and S. R. White, Unusual energy spectra of matrix product states, Phys. Rev. Lett. **134**, 126503 (2025).
- [97] M. Medenjak, B. Buča, and D. Jaksch, Isolated Heisenberg magnet as a quantum time crystal, Phys. Rev. B **102**, 041117(R) (2020).
- [98] R. J. Baxter, Exactly Solved Models in Statistical Mechanics (Academic Press, London, 1982).
- [99] D. Bhowmick, V. B. Bulchandani, and W. W. Ho, Asymmetric decay of quantum many-body scars in XYZ quantum spin chains, ArXiv:2505.05435.